Titre: Title:	Ultrasonic Tuning of Semiconductors' Band Gap
Auteur: Author:	Zahra Khani
Date:	2019
Type:	Mémoire ou thèse / Dissertation or Thesis
Référence: Citation:	Khani, Z. (2019). Ultrasonic Tuning of Semiconductors' Band Gap [Master's thesis, Polytechnique Montréal]. PolyPublie. https://publications.polymtl.ca/3958/

POLYTECHNIQUE MONTRÉAL

affiliée à l'Université de Montréal

Ultrasonic tuning of semiconductors' band gap

ZAHRA KHANI

Département de génie chimique

Mémoire présenté en vue de l'obtention du diplôme de *Maîtrise ès sciences appliquées*

Génie chimique

Février 2019

POLYTECHNIQUE MONTRÉAL

affiliée à l'Université de Montréal

Ce mémoire intitulé :

Ultrasonic tuning of semiconductors' band gap

présenté par **Zahra KHANI**

en vue de l'obtention du diplôme de *Maîtrise ès sciences appliquées*

a été dûment accepté par le jury d'examen constitué de :

Gregory PATIENCE, président

Daria Camilla BOFFITO, membre et directrice de recherche

Nick VIRGILIO, membre

DEDICATION

To my lovely family

ACKNOWLEDGMENTS

I would like to extend my sincerest thanks and appreciation to those who helped me accomplish this study.

Undoubtedly, my supervisor Dr. Daria Camilla Boffito deserves to be at the top of the list. I would like to express my appreciation to her for her kindness and patience. She has always helped to put me in the right direction during my studies, not only with her knowledge and experience but also with attitude for the high quality of research.

I would like to express my deep sense of gratitude to all my committee members for accepting to be a member of my jury, namely, Dr. Gregory Patience and Dr. Nick Virgilio.

I would like to extend my thanks to my colleagues and friends especially for sharing their friendship and knowledge with me. Special thanks go to my friends and colleagues, because of their support and friendship during my study.

Special thanks go to the secretaries and entire technical staff of the chemical engineering department.

Finally, special recognition goes out to my family, for their support, encouragement, and patience. More importantly, I would like to thank my parents who have always been there for me. Their love, support, and encouragement have been the foundation during whole my life. Without their love, unwavering support and inspiration, this work could never have been accomplished.

To my incredible sister, Maryam for encouraging me to reach the end of my potential and for believing in me. Your perseverance and hard work, your wisdom, your sense of discipline and above all, your love and patience, make you a real source of inspiration.

To my brother Khosro, who always got my back during hard times with his support and love even though we were far apart.

I dedicate this thesis to my family and sincerely seek their blessing for the path ahead.

Zahra Khani

February 2019

École Polytechnique de Montréal

RÉSUMÉ

Les eaux usées sont toutes les eaux provenant des activités domestiques, industrielles ou agricoles. Elles contiennent une grande variété de polluants physiques, chimiques et biologiques. La concentration de polluants varie en fonction de la source des eaux usées. En effet, l'activité humaine et les rejets industriels contribuent énormément au rejet des polluants dans l'eau, ce qui modifie le cycle aquatique, affectant ainsi la faune, la flore et la santé humaine.

Les chercheurs visent à mettre au point des technologies de traitement des eaux usées plus efficaces pour dégrader des polluants complexes. Cependant, l'efficacité du traitement des eaux usées dépend de leur nature et leur composition. Les processus générant des radicaux hydroxyles (Advanced Oxydation Process, AOP) sont les technologies les plus puissantes pour l'oxydation et la minéralisation des polluants organiques en dioxyde de carbone et en eau. Les AOP incluent la cavitation, l'oxydation photocatalytique et le procédé de Fenton.

En photocatalyse, la lumière irradie les semi-conducteurs et génère des espèces oxygénées réactives non sélectives (ROS) à haut pouvoir oxydant. Le dioxyde de titane (TiO_2) est le semi-conducteur le plus courant. Il est chimiquement stable, peu coûteux, non toxique, écologique et abondant. Cependant, sa large bande interdite (3,2 eV) et sa recombinaison rapide des paires électron-trou photogénérées limitent son application.

Le but de ce travail est de déterminer si la cavitation ultrasonore réduit l'énergie de la bande interdite du TiO_2 dopé au Mn sous lumière visible (de 350 nm à 750 nm). Nous avons étudié l'effet des paramètres opérationnels tels que la puissance (amplitude) et l'impulsion des ultrasons, le rapport la quantité du solvant et la température de calcination sur les propriétés des catalyseurs. De plus, nous avons synthétisé deux catalyseurs avec la méthode classique sol-gel afin de comparer les deux procédés de synthèse. La cavitation acoustique a réduit la bande interdite de 3,2 eV à 1,6 eV et a décalé la longueur d'onde d'absorbance vers la région visible du spectre électromagnétique. Tous les paramètres opérationnels ont affecté les propriétés de TiO_2 dopé au Mn. La synthèse sol-gel assistée par ultrasons a donné des poudres avec une taille de particules plus petite (inférieure à 12 µm), une surface spécifique plus élevée (supérieure à 120 $m^2\ g^{-1}$) et un volume de pores plus grand (supérieur à 0,25 cc g^{-1}) par rapport au procédé classique. L'activité des catalyseurs a été évaluée en dégradant l'acétaminophène et l'amoxicilline dans l'eau.

ABSTRACT

Wastewaters are any used water from whichever combination of domestic, industrial or agricultural activities come. Wastewaters contain a wide variety of physical, chemical and biological pollutants. The concentration of pollutants varies along with the source of the wastewaters. Indeed, human activity and industrial discharges enormously contribute to the release of pollutants in water, which in turn alter the water cycle thus affecting wildlife and human health.

Researchers aim at achieving more efficient wastewater treatment technologies to degrade complex pollutants. However, the efficiency of wastewater treatment depends on its nature and composition. Processes that generate hydroxyl radicals (Advanced Oxidation Processes, AOPs) are the most powerful technologies to oxidize and mineralize organic pollutants to carbon dioxide and water. AOPs include cavitation, photocatalytic oxidation, and Fenton process.

In photocatalysis, light irradiates semiconductors and generates unselective reactive oxygen species (ROS) with high oxidative power. Titanium dioxide (TiO_2) is the most common semiconductor. It is chemically stable, inexpensive, nontoxic, eco-friendly, and abundant. However, its large band-gap (3.2 eV) and quick recombination of the photogenerated electron-hole pairs limit its application.

The aim of this work was to assess whether ultrasonic cavitation reduces the band-gap energy of Mn-doped TiO_2 under visible light (350 nm to 750 nm). We studied the effect of operative parameters including power (amplitude), pulse, amount of solvent (mole), and calcination temperature on the properties of the catalysts. Moreover, we synthesized two catalysts with the conventional sol-gel method in order to compare the two synthetic procedures. Ultrasonic cavitation reduced the band-gap from 3.2 eV to 1.6 eV and shifted the absorbance wavelength to the visible region of the electromagnetic spectrum. All the operative parameters affected the Mn-doped TiO_2 properties. Ultrasound-assisted sol-gel synthesis yielded powders with a smaller particle size (below 12 μm), higher surface area (above 120 m^2/g) and pore volume (above 0.25 cc/g) than the conventional method. The activity of catalysts was assessed by degrading acetaminophen and amoxicillin in water.

TABLE OF CONTENTS

LIST OF TABLES

LIST OF FIGURES

LIST OF SYMBOLS AND ABBREVIATIONS

Latin alphabet

Symbol	*Definition*	*Unit*
hν	*Photon energy*	
E_g	*Energy of band-gap*	*eV*
λ	*Wavelength*	*Nm*
C	*Speed of light*	*m/s*
h	*Plank constant*	*J.s*
A_A	*Intensity XRD peak of anatase*	
A_B	*Intensity XRD peak of rutile*	
A_C	*Intensity XRD peak of brookite*	
k_A	*Contact coefficient of anatase*	
k_B	*Constant coefficient of rutile*	
τ_1	*Pulse on*	*s*
τ_2	*Pulse off*	*s*

Abbreviation

APAP	Acetaminophen
AMO	Amoxicillin
AOP	Advanced oxidation process

ROS	Reactive oxidizing species
Eg	Band gap energy
UV	Ultraviolet
US	Ultrasound
CB	Conduction band
VB	Valence band
IB	Intermediate band
XRD	X-ray diffraction
BET	Braunauer-Emmett-Teller analyze
BJH	Barret-H+Joyner-Halender method
PSD	Particle size distribution analyze
UV-vis	UltraViolet-Visible Spectroscopy analyze
HPLC	High Performance Liquid Chromatography analyze
EU	European Union
EPA	North American Environmental Protection Agency
WHO	World Health Organization
IPCS	International Program of Chemical Safety
DFT	Density functional theory

CHAPTER 1 INTRODUCTION

1.1. Context

There are many reports showing the detection of chemical pollutants, including pharmaceuticals compounds in natural water and groundwater systems. Acetaminophen (APAP) and Amoxicillin (AMO) are two of the most prescribed antibiotic, antipyretic and analgesic medicines all over the world. Even at low concentration in the range of μg L^{-1} to ng L^{-1}, they cause aquatic toxicity, genotoxicity, and endocrine disruption [1].

Various techniques are currently available to degrade organic contaminants; however, they can't remove completely pharmaceuticals from wastewater due to their high solubility, typically higher than 1000 mg L^{-1} [1, 2].

Advanced oxidation processes (AOPs) include photocatalysis, ozonation, and ultrasonication [1]. AOPs generate nonselective radicals including hydroxyl ($HO^{\bullet}$), superoxide ($O_2^{\bullet-}$), and perhydroxyl ($HOO^{\bullet}$), which oxidize organic compound and mineralize them to CO_2 and H_2O [3, 4].

Ultrasound is a sound wave that occurs at a range above the human hearing (from 20 kHz to GHz). As a sound wave, it has the characteristic of a mechanical wave. The succession of compression and expansion cycles causes the formation, growth, and collapse of cavitation bubbles. Upon collapsing, each bubble reaches 5000 K and 20 MPa, thus generating a hot spot. Chemical bonds rupture under such extreme conditions. The sonolytic thermal decomposition of organic pollutants occurs inside the bubble, at the gas-liquid interface, and/or by reaction with the reactive oxidizing species (ROS) present in solution [5].

In photocatalysis, UV light (390 nm to 750 nm) excites the electrons from the valence band to the conduction band of a semiconductor. If the photon energy of the radiation is equal to or higher than the band gap energy (E_g) of the photocatalyst, electron-hole pairs react with water to form ROS (Figure 1-1) [1, 6].

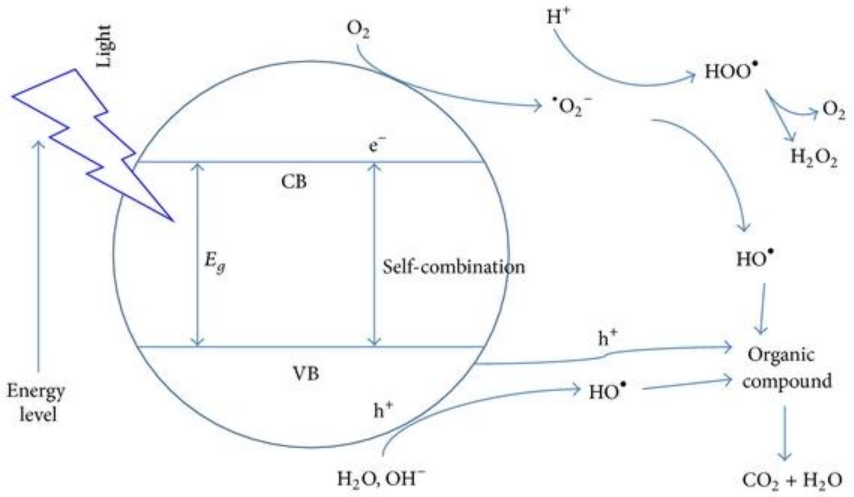

Figure 1-1. The scheme of TiO_2 photocatalytic process [taken from 7]

TiO_2 is the most applied photocatalysts due to its non-toxicity, inexpensive, chemical and thermal stability [4]. However, the application of TiO_2 is limited due to its large band gap (3.2 eV), and low quantum yield and fast recombination of electron-hole pairs. The efforts of the researches applied to modify TiO_2 materials to decrease the band gap and shift its absorption to the visible region with λ>400 nm and decrease its fast recombination of electron-hole pairs. The modification methods including doping TiO_2 with metal and nonmetal ions, and the synthesizing process and variation the operating parameters [7, 8].

Manganese, among all the 3d metals, has the potential to absorb in the visible or even infrared region of the electromagnetic spectrum, and act as a hole trap. Moreover, it is less expensive compared to noble metals [9, 10].

The synthesis of nanomaterials under sonochemical irradiation speeds the reaction rate and increases the surface area [11, 12]. In fact, acoustic cavitation increases mass transfer between the two phases and increases the diffusion coefficient [13, 14].

1.2. Objective

The general objective of this research is to assess whether ultrasound can decrease the band-gap of TiO_2-MnO_x. If so, to improve the band-gap of the catalysts and extend the absorption edge of catalysts. We synthesized Mn-doped TiO_2 catalysts by ultrasound assisted sol-gel method and assessed the effect of power, pulse, and solvent quantity. XRD, BET, PSD, and UV-spectrophotometer characterized our samples. We compared the physicochemical properties of the samples obtained with ultrasound-assisted sol-gel and conventional sol-gel process. Also, the combination of ultrasound and ultraviolet irradiation with the synthesized catalyst used to degrade acetaminophen and amoxicillin

1.3. Plan of the dissertation

This master's dissertation is divided into five chapters. Chapter 2 presents the literature review and theoretical aspects of advanced oxidation process and catalyst preparation methods. Chapter 3 describes experimental and analytical procedures along with the facilities implemented in this study. Chapter 4 presents a summary of the main results of this work in the form of a scientific article most recently submitted for publication in a scientific journal. General discussion is presented in chapter 5 and finally conclusion and the future recommendation are presented in Chapter 6.

CHAPTER 2 LITERATURE REVIEW AND THEORETICAL ASPECTS OF ADVANCED OXIDATION PROCESS

2.1. Introduction

Advanced oxidation processes (AOPs) effectively mineralize a variety of organics into CO_2, H_2O or mineral acids [13-15]. AOPs remove pollutant through the generation of highly oxidative radical species, including hydroxyl ($HO^{\bullet}$), superoxide ($O_2^{\bullet-}$), and perhydroxyl ($HOO^{\bullet}$) radicals. Advanced oxidation processes include 1) ozone treatment, 2) photocatalysis, 3) ultrasonic cavitation [8].

2.1.1. Ozonation

Ozone with the oxidation power of (2.07 V) degrades organic pollutants (1) indirectly by hydroxyl radical (OH^-), or (2) directly by electrophilic attach by molecular ozone. In the water and wastewater treatment, ozonation is one of the effective methods for degradation organic pollutants. However, some disadvantages such as slow and incomplete oxidation processes, low utilization rate because of its low solubility and stability in water limit its application. Researchers made efforts to overcome these problems [8].

2.1.2. Photocatalysis

Photocatalytic processes degrade pollutants through catalysis at ambient temperature and pressure [8]. One of the main advantages of the photocatalytic process compared to the other AOPs processes is the generation of a renewable oxidant source [4].

In photocatalyst processes semiconductor catalysts degrade organic materials such as dyes and pharmaceutical compounds [15]. Titanium dioxide (TiO_2) and zinc oxide (ZnO) are two important and successful photocatalysts because of their resistance to acidic or alkaline conditions, good photosensitivity and chemical stability, economically, abundant, non-toxic, and the strong

oxidizing power of their holes [8, 16-18]. TiO_2 is the common catalyst in the applications including water and air purification, sterilization, self-cleaning, defogging, and H_2 generation. Compared to the other semiconductors, TiO_2 is more stable photo-chemically and chemically [8]. Rutile (tetragonal), anatase (tetragonal), and brookite (orthorhombic) are three crystalline phases of titanium dioxide (Figure 2-1) [8]. Anatase has the highest photocatalytic activity while rutile is the most stable phase [19].

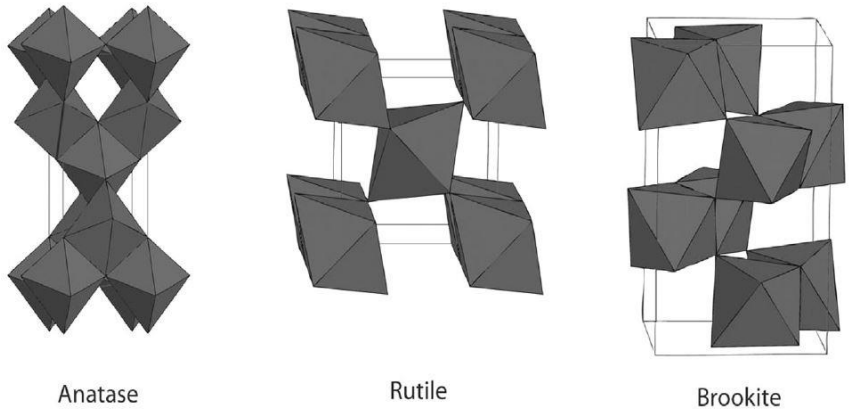

Figure 2-1. TiO_2 crystal structure Anatase, Rutile and Brookite [taken 8]**.**

The photocatalyst absorbs photon energy (hv), which is equal to or higher than the photocatalyst's band-gap, to excite electrons [16]. Then the process starts with exciting electrons from the valence band to transfer an electron to the conduction band and it generates an electron-hole pair (e^--h^+). The reaction between electron-hole pair and water and oxygen molecules produces the hydroxyl radicals ($OH^\bullet$) and superoxide anions ($O_2^{\bullet-}$) [8, 20].

The whole excitation process is in four steps, 1) photoexcitation, 2) charge-carrier trapping of e^-, 3) charge-carrier trapping of h+, and 4) electron-hole recombination:

$$TiO_{2\,(aq)} + h\nu \rightarrow e^- + h^+ \quad (1)$$

$$e_{CB}^- \rightarrow e_{TR}^- \quad (2)$$

$$h_{VB}^+ \rightarrow h_{TR}^+ \quad (3)$$

$$e_{TR}^- + h_{VB}^+ \,(h_{TR}^+) \rightarrow e_{CB}^- + heat \quad (4)$$

The conduction band energy of TiO_2 is slightly higher than the reduction potential of oxygen (E_{CB}=0.51 V, E_o=-0.33 V), therefore, oxygen molecules through a reduction process trap electrons in the conduction band, which produce superoxide radical anions (O_2^-). Water ionization generates H^+ that will protonate the superoxide. $HOO^\bullet$ produces HO_2^- by trapping another electron and HO_2^- generates hydroxyl peroxide. Finally, hydrogen peroxide will decompose to hydroxyl radicals ($OH^\bullet$) [8].

$$(O_2)_{ads} + e^- \rightarrow O_2^{-\bullet} \quad (5)$$

$$O_2^{-\bullet} + H^+ \rightarrow HOO^\bullet \quad (6)$$

$$H_2O \rightarrow OH^- + H^+ \quad (7)$$

$$HOO^\bullet + e^- \rightarrow HO_2^- \quad (8)$$

$$HO_2^- + H^+ \rightarrow H_2O_2 \quad (9)$$

$$H_2O_2 + e^- \rightarrow OH^- + OH^\bullet \quad (10)$$

$$H_2O + h^+ \rightarrow H^+ + OH^\bullet \quad (11)$$

Hydroxyl radicals, electrons, holes and other oxidizing radicals can deactivate or decompose organic and inorganic pollutants [8].

Generally, organic compounds decompose into carbon dioxide and water in the presence of TiO_2 and irradiation of UV light. Increasing the specific surface area by decreasing the particle size of the catalyst is key to improve TiO_2 photocatalytic activity [21, 22].

TiO_2 is highly active under UV light irradiation, however, its large band gap (E_g= 3-3.2 eV) and low quantum yield limit its application under visible light. With the fact that the visible light is the major part of the solar energy, it is better to use solar light in the visible region [20].

Different TiO_2 structures have different oxidation power (3.0 eV for rutile and 3.2 eV for anatase). The light wavelength below 400 nm excites this photocatalyst. When the UV light irradiates on the TiO_2, it will generate electrons (e^-) and holes (h^+) in conduction (CB) and valence band (VB), respectively [8, 23].

Another limitation of using TiO_2 is its fast recombination of electron-hole pairs. However, coupling two semiconductors improve their photoactivity, delay their fast charge recombination and shift the light absorption to the visible light region [8, 24].

Dopant materials are transition metals including, Fe, Mn, Zn, Ni, Cr, Co, W, Zr, Ce, and V, noble metals including Au and Pt, metal oxides such as Fe_2O_3, Cr_2O_3, MgO, CaO, and SiO_2, and non-metals including N, S, C, and B. Doping these materials with TiO_2 extend its adsorption to a longer wavelength [7, 23, 25-27].

Doping TiO_2 with transition metal ions introduces intra-band gap state that decreases in the band gap energy by introducing the interaction between the 3d orbital of Ti and the d orbital of a transition metal. On the other hand, metal dopants prevent electron/hole recombination by merging in the crystal lattice of TiO_2, which increase the photoactivity of TiO_2 doped with metals [28-30].

Fe^{3+} among the other metal ions has several advantages including non-toxicity, inexpensive, easily incorporated into the crystal lattice of TiO_2, and it has the same radius as Ti^{4+} (Fe (0.79 Å) and Ti^{4+} (0.75 Å)). One of the successful examples of using TiO_2-Fe is decomposition dye by photocatalytic degradation. Fe-doped TiO_2 or rGO-doped TiO_2 reduces band-gap from 3.2 eV (TiO_2) to 2.40 eV (TiO_2-Fe) and 2.85 eV (TiO_2-rGO) [14]. TiO_2-rGO is more photocatalytically active to remove pharmaceutical, while, TiO_2-Fe is more active under visible light, TiO_2-Fe catalysts remove 57% of ibuprofen, 46% of carbamazepine, and 35% of sulfamethoxazole after 6 h [7]. Among all the dopants, Mn is inexpensive and both Mn^{3+} and Mn^{4+} can act as a hole trap [9]. Mn has the potential of optical absorption in the visible region or even the infrared solar light. The combined effect of the intermediate bands (IBs) and narrowed band gap within the forbidden gap enable Mn to move the absorption to the visible region [32-34].

2.1.3. Ultrasound

Acoustic cavitation is the main part of the ultrasonication. Cavitation classified into four different categories based on its generation (acoustic cavitation, hydrodynamic cavitation, optic cavitation, and particle cavitation). Acoustic cavitation and hydrodynamic cavitation are the most applied cavitation in industry and academia. Acoustic cavitation occurs by using high-frequency sound waves, normally ultrasound with the frequencies in the range of 20 kHz to 100 MHz [35].

Mechanical vibration of the ultrasonic wave in a liquid produces a cycle of expansion and compression phases. Compression applies a positive pressure and forces molecules to put together, while expansion exerts negative pressure and force molecules to separate. Two different cavitation phenomena will occur:

Stable cavitation: when the acoustic intensity is low, bubbles grow slowly over acoustic cycles. Since the bubble size variation is small, the chemical effect in this process is not significant.

Transient cavitation: high acoustic intensity causes the growth and collapse of bubbles during the cycle of an ultrasonic wave. The bubbles size increases and collapse extremely in less than a microsecond.

The intensity of the sound wave, the solvent characteristics, gas properties, and temperature affect the cavitation and bubbles collapse [36].

The produced cavitation bubbles grow and collapse violently and generate hot spots with extremely high temperature and pressure up to 5000 K and 20 MPa, respectively and very high cooling rate ($>10^{11}$ K s^{-1}). Collapsing the cavitation bubbles followed by several reactions including pyrolysis inside the bubble and the reaction with the radicals at the interface of bubble-liquid or in liquid bulk [28]. These conditions depend on several factors that include intensity and frequency of irradiation [37-39]. The collapse of microbubbles releases energy that causes the formation of reactive hydrogen atoms and hydroxyl radicals which leads to recombination and formation of hydrogen peroxides. The reactions during acoustic cavitation are as follow:

$$H_2O \rightarrow H^{\bullet} + HO^{\bullet} \quad (16)$$

$$O_2 \rightarrow 2O \quad (17)$$

$$H + O_2 \rightarrow HOO^{\bullet} \quad (18)$$

$$O + H_2O \rightarrow 2HO^{\bullet} \quad (19)$$

$$H + O_2 \rightarrow HO^{\bullet} + O \quad (20)$$

The unreacted radicals with the substrate can transform to hydrogen peroxide:

$$2HO^{\bullet} \rightarrow H_2O_2 \quad (21)$$

$$2HOO^{\bullet} \rightarrow H_2O_2 + O_2 \quad (22)$$

The sonochemical process is an effective method to remove chemical compounds in the micro to the milli-molar range [15, 29, 35]. The sonochemical reaction consists of two pathways for degradation of organic compounds, (1) during the collapsing cycle of bubbles, volatile compounds evaporate and degrade via pyrolytic reaction; and (2) the reaction between OH radicals with organic compounds, adsorb on the bubble surface [5, 40, 41].

2.1.4. Combination of AOPs

Single water treatment process encounters several difficulties, mostly related to technical unavailability and incomplete removal of target pollutants. Therefore, combined or integrated technologies have been increasingly applied over the last years, in which the main advantages of individual processes are enhanced by the beneficial effects of their counterpart, while downsides are overcome.

Reports showed that combining ultrasound and ultraviolet irradiation with both homogeneous and heterogeneous photocatalysis increase the efficiency of removing pollutants. The principle process of two systems is producing OH radicals, which are powerful oxidizing species. The combination of these two processes increases the degradation of the contaminants [41]. Also, sonochemical oxidation combined with photocatalysis prevents aggregation of the catalyst during photocatalysis and the effect of acoustic cavitation keeps the surface of the catalyst constantly clean [29].

2.2. Catalyst preparation methods

Precipitation, wet impregnation, sol-gel, hydrothermal process, electrochemical method, ultrasound process are processes to synthesize nanoparticles. However, most of the conventional methods have a few drawbacks including the inability to obtain particles with controlled size distribution, with sizes of 100 nm or above, which may not meet requirements for some specific applications. Furthermore, these methods have multiple steps and require a long time [13,42]. Changing operative parameters during the synthetic procedure control shape, size, and composition of the catalyst [20].

The sol-gel process applied mostly for making nanomaterials [42]. Ultrasound is one of the newest synthesizing processes for a wide range of nanostructured materials, including high-surface area transition metals, alloys, carbides, oxides, and colloids [34]. One of the key factors in the synthesis of crystalline TiO_2 at a lower temperature is to have a longer aging time. The smaller the particle sizes, the higher the photocatalytic activity [11, 19].

Hereunder, a brief description of some of the synthetic processes:

2.2.1. Precipitation

Precipitation starts with the addition of the precipitating agent to a solution of metal salt to generate a precipitate. Then the precipitate undergoes washing, drying, and calcination. Coprecipitation prepares composite materials by using different cations such as Si, Co, Mn, Cu, Ni, and Al. Various parameters including precipitation temperature, the type of precipitating agent and its concentration, precipitation pH, stirring speed and feeding order to affect the characteristics of the final products. Therefore, the operative conditions should be optimized to obtain the best results [43].

2.2.2. Wet impregnation

Wet impregnation widely applies to the preparation of supported catalysts. The oxide material is immersed into a solution containing dopant precursor, then the mixture undergoes heating and drying. Wet impregnation is one of the most exploited methods to synthesize supported Fe based catalyst including Fe_2O_3/Al_2O_3, Fe_3O_4-CoO/Al_2O_3, Fe-Co/ZrO_2, and Pd/FeOOH [43].

2.2.3. Hydrothermal method

The hydrothermal method uses water as a solvent. The process occurs at high pressure and temperature [15]. One of the advantages of this process is that at high temperature (above 100 ^oC) it overcomes the agglomeration and produce powders with high purity, good dispersion, precise control of pore structure and well crystal shape. The operative parameters solvent type,

temperature, and process time affects the synthesis of the products. Temperature controls the production rate if other parameters are constant [26].

2.2.4. Sol-gel

Sol-gel synthetic procedures yield particles with high photocatalytic activity [16]. The sol-gel process is the evolution of sol to gel, then transfer the gel to crystalline materials [44]. The reaction of hydrolysis and polycondensation in the sol-gel process are the main reaction to prepare TiO_2 [16]. The flexibility of control over pore structures is one of the advantages of this process [17]. The sol-gel process produces amorphous particles that require further treatment to convert to a crystalline form [14]. The reaction temperature, reaction time and method of preparation affect the crystallization process [14].

Hydrolysis

$$M(OR)_n + H_2O \rightarrow M(OR)_{n-1}(OH) + ROH \quad (12)$$

Condensation

Dehydration:

$$M(OR)_n + M(OR)_{n-1}(OH) \rightarrow M_2O(OR)_{2n-2} + ROH \quad (13)$$

Dealcoholation:

$$2M(OR)_{n-1}(OH) \rightarrow M_2O(OR)_{2n-2} + H_2O \quad (14)$$

The overall reaction is:

$$M(OR)_n + \frac{n}{2} H_2O \rightarrow MO_{n/2} + nROH \quad (15)$$

Control the part of hydrolysis to obtain homogeneous titanium oxide is necessary. Gelation and calcination follow condensation [16]. Dehydration and calcination transform amorphous gel into crystalline solid. Calcination converts the hydroxide complex into the final metal oxide. The calcination temperature and time have the most influence on the properties of the synthesized materials [42]. Although, at the very high-temperature the particles will aggregate, and it affects the microstructures of the TiO_2 particles. The microstructure of TiO_2 defines its photocatalytic

activity [16]. Calcination time controls the phase transformation. Slow calcination process allows the lattices to orient properly and creates well microstructure and crystalline materials [42]. The crystal structure of TiO_2 affects its photocatalytic activity. Anatase is more active than rutile. An anatase/rutile ratio of 7/3 gives the best photocatalytic activity for wastewater treatment.

2.2.5. Ultrasound-assisted by sol-gel process

The application of ultrasonic cavitation to the conventional sol-gel method entails the formation of equally sized nanoparticles and prevents agglomeration. Ultrasound prepares many nanostructured materials such as high-surface area transition metals, alloys, carbides, oxides [23, 45]. Ultrasound irradiation accelerates chemical reactions that would not occur under normal conditions [12, 46]. Acoustic cavitation syhnthesize particles and prevents metal atoms agglomeration [29].

The hot spot mechanism is one of the theories that explain how the collapse of bubbles breaks down the chemical bonds. Regarding this theory, each collapsing bubble reaches a very high temperature (5000-2500 K) and very high cooling rates (10^{11} K/s). Very high cooling rates prevent crystallization [47].

Ultrasonic cavitation process is more applicable to control over size, morphology, and dispersion of the metal components than the conventional sol-gel process. Also, the conventional sol-gel process requires longer process times than the ultrasound-assisted one. Acoustic cavitation also improves the properties of the catalyst, enhance the surface area, control particle size distribution and finally improve photocatalytic activity [29]. Overall, optimizing the operative parameters makes the cavitation process as efficient as possible [44]. Sonication time is one of the important parameters which can influence the crystallite size and crystallinity of the synthesized nanoparticles [42]. Pinjari, D. V., et al., studied the effect of calcination and sonication time on the crystallinity of the TiO_2. Increasing sonication time, increases the content of rutile until it reaches the optimum value, then beyond that due to the collapse of bubbles, it will decrease the rutile content [42]. The ultrasound irradiation time, temperature, power density, the ultrasonic sources (bath-type and horn-type), magnetic stirring and size of the reactor affect the characteristic of the synthesized catalysts [48].

Although the formation of nanostructured material is still unclear, there are two explanation for the formation of amorphous products. The first one is related to the fast kinetics that does not allow the nuclei to grow. In each collapsing bubbles, a new nucleation center will form, however the short cavity collapse time and incoming acoustic waves limit their growth. According to the second explanation, a non-volatile precursor causes the main reaction occurs inside the liquid phase instead of inside the collapsing cavity. Based on the temperature in the fluid spherical shell region where the reaction occurs, amorphous particle or nano-crystalline will form [12].

The advantages of ultrasound-assisted nanoparticles synthesis are:

Preparation of amorphous products: acoustic cavitation to synthesize amorphous metal oxides, does not require the addition of a glass former.

Insertion of nanomaterials into mesoporous materials: ultrasonic waves transfer amorphous nanosized catalysts into mesopores. Nanoparticles are deposited on the inner mesopores walls, without blocking them. Comparing this method to others such as impregnation or thermal spreading, sonochemistry produce products with better properties.

Deposition of nanoparticles on ceramic and/or polymeric surfaces: acoustic cavitation for deposition of nanoparticles (metals, metal oxides, and semiconductors) on ceramic or polymer surface yields a homogenous and smooth coating layer on the surface. The nanoparticles cannot be removed by washing because of the chemical bonds with the substrate.

The formation of proteinaceous micro- and nanosphere: sonication converts any protein into the sphere and it causes encapsulation of a drug in the sphere. The obtained spherical proteins are biologically active [12].

2.3. The literature review on TiO_2-MnO_2

Authors	Studied parameters and effect	Reference
Stucchi, M., et al.	They doped Mn with TiO_2 with ultrasound assisted method and conventional sol-gel process. They showed that ultrasound assisted process increases the surface area, porosity compared to conventional process.	[9]

Jimmy, C. Yu, et al.,	They synthesized TiO_2 in 1:1 EtOH-H2O solution under ultrasonic irradiation and compared with sample prepared with conventional sol-gel process. Their result showed ultrasound process cause catalyst with higher photocatalytic activity, surface area, porosity, pore volume and smaller pore size compared to conventional sol-gel process.	[11]
Prasad, Krishnamurthy, et al.,	They applied both conventional and sonochemical method to synthesize their catalyst. The ultrasound assisted (US) process synthesized thermally stable catalyst at lower operation time. Moreover, ultrasound cause more rapid phase transformation.	[12]
Shirsath, S. R., et al.	Fe and Ce doped with TiO_2 by sonochemical process and conventional sol-gel process. They report that catalyst synthesized with ultrasound showed higher photocatalytic activity, and the amount of the dopant affect photocatalytic activity of the catalysts.	[13]
Huang et al.	Synthesized and characterized Fe_xO_y-TiO_2 via sonochemical method. They investigated the effect of the temperature and the precursor on the particle size. They obtained particle with maximum size of 9 nm and they showed the relevant effect of these two parameters on the particle size.	[19]
Li, Haibin, et al.	They synthesized nanosheets of Ag-TiO_2 by ultrasound. They showed the synthesized catalyst have the potential to work under solar light.	[22]
Shi, Zhongliang, et al.	They used Fe and Ce as dopant, and they investigated the effect of Fe and Ce as dopant. They claimed that the synergistic actions of the two dopants improved the photocatalytic activity of the catalyst.	[24]
Shende, T. P., et al.,	Graphene oxide (GO) prepared in the presence of ultrasound irradiation.	[45]
Tripathi, Anand Kumar, et al.,	They synthesized Sn and Mn doped TiO_2 nanostructures by sol-gel method. They indicated that the optical band-gap for these catalyst designated red-shift.	[49]
Yu, Jiaguo, et al.	An ultrasound-assisted process was used to synthesize mesoporous titanium dioxide. They claimed that the photocatalytic activity of the sample prepared with ultrasound is higher that the commercial Degussa P25 and the sample prepared by conventional hydrolysis method.	[50]
Zhou, M., Yu, J., & Cheng, B.	An ultrasound-assisted process was applied to synthesize Fe-doped TiO_2 catalyst. The result showed that small amount of Fe^{3+} ions can increase the photocatalytic activity of the catalysts.	[51]
Neppolian, B., et al.	They applied ultrasound-assisted sol-gel process to synthesize Nano-size TiO_2 photocatalysts. They studied the effect of six operative parameters of ultrasonic irradiation time, power density, ultrasound sources, magnetic	[52]

	stirring, initial temperature and the reactor on the photocatalytic properties of the synthesized catalyst.	
Li, Haibin, et al.	They synthesized Fe doped TiO_2 with an ultrasonic-hydrothermal method. They combined two process in order to reach large specific surface area, high crystallinity, and high thermal stability.	[53]
Stucchi, M., et al.	They deposit Ag nanoparticles on the surface of the TiO_2 under ultrasound irradiation. They investigated effect of the amount of the Ag on the photocatalytic activity of the catalyst and the band-gap of the catalyst.	[54]

CHAPTER 3 EXPERIMENTAL METHODOLOGY

3.1. Materials

We employed the following material to synthesize Mn-doped TiO_2: Ti(IV)-butoxide (Ti(IV)-buOX, reagent grade, 97%), manganese (II) nitrate hydrate ($Mn(NO_3)_2 \cdot xH_2O$, 98%), nitric acid (HNO_3, ACS reagent, 70%), ethanol (EtOH, absolute, for HPLC, ≥98%), and methanol was the eluent for the HPLC (CH_3OH, for HPLC, ≥99.9%). All the reagents were from Sigma Aldrich and used without any further purification.

3.2. Synthesis

A 500W ultrasonic processor applied to synthesize Mn-doped TiO_2 catalysts by ultrasound assisted sol-gel method (Table 3-1). We applied the factorial design based on three operating parameters: power (amplitude), pulse, and water:ethanol mole ratio (Table 3-2). We applied a probe equipped with a 20 mm diameter replaceable tip. The replaceable tip was kept at 2 cm above the bottom of the reactor. In order to work at constant power, we calibrated the ultrasonic processor periodically. For the calibration, the slope of the curve (temperature (°C) vs time (s)) was multiplied by the grams of the water used in the system and by 4.19 J/cal. The results gave the Watts of ultrasonic energy expanded in the working liquid over the calibration period. We calculated for four amplitude and finally, the curve of ultrasonic power vs the corresponding amplitude gave the calibration line of the ultrasound. By starting the sonication, we added the mixture of water and $Mn(NO_3)_2$ dropwise to the solution mixture of titanium (IV) butoxide, ethanol, and HNO_3. Ultrasound irradiated the solution for 3 h 30 mins. Afterward, the gels aged at room temperature before drying overnight at 100 °C. For investigating the effect of calcination temperature two of the samples calcined at 550 °C for 5 h (Table 3-3). Two samples were prepared by a conventional sol-gel method in order to compare the ultrasonic cavitation and conventional sol-gel process (Table 3-4). The samples aged and dried at 100 °C overnight. Calcination temperatures were 450 °C and 550 °C.

Table 3-1. Ultrasonic processor specifications

Parameter	Specification
Tip material	Titanium alloy (Ti-6Al-4V)
Tip diameter	13 mm
Probe length	136 mm
Processor power	500 W
Processor frequency	20 kHz

Table 3-2. Experimental design; factorial design

Samples name	Power (W)	Solvent (mole)	Pulse (s)
TM10-49-0	10	49	0-0
TM10-195-1	10	195	1-1
TM10-98-2	10	98	2-2
TM20-195-0	20	195	0-0
TM20-98-1	20	98	1-1
TM20-49-2	20	49	2-2
TM30-98-0	30	98	0-0
TM30-49-1	30	49	1-1
TM30-195-2	30	195	2-2

Table 3-3. Synthetic conditions of sample 4 and 9 calcined at 550°C

Samples name	Power (W)	Solvent (mole)	Pulse (s)	Calcination temperature (°C)
TM20-195-0	20	195	0-0	550
TM30-195-2	30	195	2-2	550

Table 3-4. Synthetic conditions of the conventional sol-gel method, sol-gel stirred at 400 rpm

Samples name	Solvent (mole)	Calcination temperature (°C)
Sol-gel-450	195	450
Sol-gel-550	195	550

3.3. Analytical

X-ray diffraction is applied to determine phase equilibria and crystal structure. Monochromatic radiation (single wavelength x-rays) due to their high intensity are ideal for XRD analysis. The main concept of XRD analysis include X-rays, crystals, and diffraction. When light is scattered by a periodic array, produce constructive interposition at specific angles and produce diffraction. The diffraction pattern is the plot of the intensity vs. the angle of the detector, 2θ.

The arranged atoms in a crystal diffract the light with the wavelength equal to the distance between their atoms. The X-rays provides a diffraction pattern that contains information on the atomic arrangement in crystal [55].

The diffraction is calculated by the Bragg's law as follow [56]:

$$2dsin\theta=n\lambda \quad (16)$$

Where λ is the wavelength of the incident X-rays, θ is the incident angle of the beam and d is the spacing between the crystal lattice planes of atoms. Then we can define the phases of the obtained material by comparing the diffraction with the database of the known diffraction [56].

We obtained X-ray diffraction (XRD) patterns on a Philips PANanalytical (USA) X'pert diffractometer at ambient temperature with an angle of incidence of 0.5° and Cu Kα (1.5406 Å) radiation at 50 kV and 40 mA. The instrument scanned the diffraction angle between 0° and 80°, with a divergence slit of 1°.

The basis of the BET is associated with the gas adsorption on the surface of the materials. The adsorption process can be physical or chemical. The physical adsorption is based on the van der Waals forces however in chemical adsorption, there is an interaction between the gas and the materials. The amount of the gas adsorbed on the surface of the material indicates the surface area. The BET theory is related to the Langmuir theory. The BET theory is based on the multilayer adsorption that all the layers are in equilibrium and there is no interaction between layers, therefore the Langmuir equation applied for each layer [57].

Nitrogen adsorption in an AUTOSORB-1 (Quantachrome Instruments, USA) by the standard multi-point Brunauer–Emmett–Teller (BET) analyzed the powder sample analyzed. The as-prepared powder sample was degassed at 200 ◦C. The BET surface area was determined by the multipoint BET method, desorption isotherm was used to determine the pore size distribution using the Barret–Joyner–Halender (BJH) method with cylindrical pore size.

Light scattering method measures the particle size distribution based on different theories, which one of them is the Mie theory. The Mie theory predicts the intensity of scattered light as a function of particle size, the angle of observation, and wavelength and polarization of the incident beam [58].

By using the Mie algorithm with a laser scattering analyzer (LA-950 Horiba, China), the particle size distribution (PSD) were analyzed.

Spectroscopy is based on the interaction between the light with the matters. As a result of light absorption by material, the energy of the atoms or molecules increases. Chemical compound by absorbing light produces a distinct spectrum. The absorbed light excites the electrons from the ground towards a higher energy state. The absorbed light is equal to the energy differences between the higher energy and the ground state [59].

We performed the UV-vis band-gap analysis to measure the band-gap of the Mn-doped TiO_2 catalysts. We calculated the band-gap (E_g) of each sample with the Plank's equation [60]:

$$E_g = hc/\lambda \quad (23)$$

Whereas h is 6.63 E-34 J.s, c is the light speed of 3.0 E+08 $msec^{-1}$ and λ is the cut-off wavelength in nm. For measuring λ we used a Thermoscientific UV–VIS Evolution 300 spectrophotometer equipped with a diffuse reflectance accessory (Pike technology EasiDiff) in the wavelength range of 200-900 nm.

3.4. Drug adsorption

In order to verify the photocatalytic capability of the prepared samples, we examined them in a sono-photocatalytic reaction. We prepared the solution of 0.1 g L^{-1}, 150 mL water and 25 ppm of acetaminophen or 100 ppm of amoxicillin and used the continuous sonication and ultraviolet irradiation for 3 h to degrade acetaminophen and amoxicillin. We employed a jacketed glass reactor and tap water to keep the temperature of the reaction low.

UVA lamp was kept in a distance of the reactor to give the irradiation intensity of 160 Wm^{-2}. We sampled every 30 min for the HPLC analysis. A Varian Prostar HPLC instrument (model 210, series n. 04,395), equipped with a Prostar 410 Auto-sampler control and a C-18 column (Microsorb MW 100-5 C18, 250×4.6, Variant, Agilent Technologies) analyzed the concentration of the acetaminophen and amoxicillin contaminants. Before analyzing the experiments, we calibrated the instrument for both contaminants with the analytical method. In both cases, the mobile phase consisted of MeOH and H_2O (HPLC grade) in a 25:75 ratio at a constant flow rate of 0.5 ml min^{-1}. The detection wavelength (λ) for acetaminophen and amoxicillin were 210 and 275 nm, respectively.

CHAPTER 4 ARTICLE 1: ULTRASOUND TUNES THE BAND-GAP OF MnOx-TiO_2 SYSTEMS

Zahra Khani[1], Dalma Schieppati[1], Claudia L. Bianchi[2], Daria C. Boffito[1]

[1] Chemical Engineering Department, Polytechnique Montréal, C.P. 6079, Succ. CV Montréal, H3C 3A7, Québec, Canada

[2] Dipartimento di Chimica, Università degli Studi di Milano, via Golgi 19, 20133 Milano, Italia

Submitted to Ultrasonic chemistry journal in February 2019

This article presents the main results of the research project.

Abstract

Advanced Oxidation Processes are the most powerful technologies to degrade organic pollutants, including pharmaceuticals, to carbon dioxide and water.

TiO_2 is the most employed semiconductor and yet it features a high band gap energy (3.2 eV) and fast electron-hole pair recombination. When Mn is embedded in TiO_2, it shifts the absorption wavelength of TiO_2 towards the visible region of the electromagnetic spectrum.

Ultrasound assists the sol-gel process by increasing the surface area and pore volume of TiO_2, thus increasing the photoactivity of the semiconductor when exposed to UV visible radiation.

In the present work, we studied the effect of the ultrasonic power, pulse, and solvent quantity on the particle size and structure of Mn-doped TiO_2. The ultrasound-assisted synthesis of semiconductors yielded mesoporous Mn-TiO_2 powders with a higher surface area (158 m^2 g^{-1}) and pore volume (0.29 cc g^{-1}), and smaller particle size (4 µm) than those obtained with the conventional sol-gel method (181 µm). We assessed the activity of Mn-doped semiconductors via the sonophotocatalysis of amoxicillin and acetaminophen in water.

Keywords:

Ultrasound, photocatalysis, synthesis, amoxicillin, acetaminophen, TiO_2

4.1. Introduction

The effort to reduce chemical pollutants from water resources is a widespread issue [1], [2].

Improper disposal of drugs, illicit discharge during manufacturing, and the direct or indirect release by humans and animals are the main causes of water contamination [3], [4]. These contaminants damage the ecosystem even in the range of ng L^{-1} to µg L^{-1}. They interfere with the endocrine system of complex organisms, induce microbiological resistance, and accumulates in soil and plants [3], [5], [6]. Many governmental and non-governmental organizations including European Union (EU), the World Health Organization (WHO), and the International Program of Chemical Safety (IPCS) provide rules and legal frameworks to protect and improve the quality of the resources and investigate the long-term effects of these contaminants, which still need further investigation [5]. Antibiotics, anti-inflammatories, hormones, blood lipid regulators, analgesics, lipid regulators and many other recalcitrant pharmaceuticals pollute water at g L^{-1} order of magnitude [7].

Two of the most prescribed analgesics and antibiotics are acetaminophen (APAP) and amoxicillin (AMO), respectively [4], [8]. APAP concentration in several treatments plants effluents is higher than 200 µg L^{-1}, which causes liver-related pathologies and other severe ailments [9]–[12]. Moreover, antibiotics consumption is expected to grow by 67 % in the next five years [3].

Various techniques are currently available to degrade organic contaminants. Specifically, advanced oxidation processes (AOPs) mineralize a wide variety of organics into CO_2, H_2O and/or mineral acids [15]–[16]. AOPs remove pollutants through the generation of highly oxidative radical species, namely hydroxyl ($HO^{\bullet}$), superoxide ($O_2^{\bullet-}$), and perhydroxyl ($HOO^{\bullet}$) radicals. AOPs include 1) ozonation, 2) photocatalysis, and 3) ultrasonic cavitation [15]. In addition, the combination of UV radiation with ultrasonication increases the efficiency of removing contaminants from water [16]

One of the major advantages of photocatalysis over other AOPs is the generation of renewable oxidant sources as other AOPs use consumable oxidants [12]. The efforts of researchers aim at improving the properties of catalysts in order to enlarge the band gap to the visible light region of the solar spectrum (λ>400 nm). Modifications include doping with metal or non-metal ions and a wide variety of diverse synthetic procedures. The shape and size of catalysts vary with the operative parameters including the ultrasound irradiation time, temperature, power density, the

ultrasonic sources (bath-type and horn-type), magnetic stirring, and reactor shape and size [13], [17], [18].

TiO_2 is one of the most employed semiconductors. It applies to water and air purification, sterilization, self-cleaning, defogging, and H_2 generation. TiO_2 is cheaper and more photo-chemically and chemically stable than other semiconductors [15]. It efficiently degrades organic dyes and pesticides when exposed to ultraviolet radiation [19], [16].

However, TiO_2 large band gap (from 3.0 eV to 3.2 eV), low quantum yield and fast recombination of electron-hole pairs limit its application under visible light. Metals, metal oxides and non-metals doping extends the absorption of TiO_2 to a longer wavelength [13], [20]–[23].

In previous studies, Stucchi et al. investigated the effect of ultrasonication on the activity of Ag-doped TiO_2 photocatalysis degradation of acetone under UV light. Ag makes TiO_2 active under visible light [24]. They also showed that doping TiO_2 with Manganese shifts the absorption towards the visible light region of the electromagnetic spectrum [25].

Among all the 3d metals, Mn has the potential of optical absorption in the visible region or even the infrared solar light [26]–[28]. Doping TiO_2 with Mn introduces considerable energetic elevation that causes the energy gap to narrow [28] and it enhances the crystallinity of the material [29]. Metals and metal oxides form new electronic states between the valence and conduction band of TiO_2 and gap and reduce the electron-hole recombination rate by acting as an electron trap. This is due to the interaction between the 3d orbital of Ti and the d orbital of Mn. Therefore, the distance of charge transfer between electrons of the Mn ions and the conduction or valence band of TiO_2 is narrowed and the introduced intra-band gap shifts the absorption edge towards the visible region [30]. Moreover, the intra-gap creates new electronic states in the TiO_2 band gap, which promotes the d electron transfer from Mn to the conduction band of TiO_2 [29].

The conventional sol-gel synthetic procedure requires a long processing time. Ultrasonic cavitation is a faster and effective method to synthetize TiO_2 [31]. Ultrasound is a mechanical wave that propagates through a succession of compression and rarefaction cycles. This results in the formation of vapour-filled voids that grow and collapse violently to generate hotspots wherein the temperature and pressure reach up to 5000 K and 20 MPa, respectively. The application of

ultrasound lowers the process temperature and yet facilitates the transition from amorphous to crystalline structure [32].

Acoustic cavitation increases the surface area, controls the particle size distribution and finally improves photocatalytic activity [33]. The optimization of the sonication parameters is essential to generate particles with specific characteristics [31].

Neppolian et al. [34] prepared Nano TiO_2 photocatalysts using sol-gel and ultrasound-assisted sol-gel methods. They investigated the effect of ultrasonic irradiation time, power density, ultrasonic source, magnetic stirring, initial temperature and geometry of the reactor. Li et al. [19] combined ultrasonic cavitation and hydrothermal method to prepare Fe-doped TiO_2 for the photo-degradation of methyl orange (MO). The high crystallinity, large surface area and larger pore size of the prepared samples resulted in 2.5 times faster photodegradation of MO. Prasad et al. [31] proved that ultrasound sped up the synthesis and minimized agglomeration in the synthesis of ZrO_2.

The objective of this work presents its originality. We synthesized Mn-doped TiO_2 catalysts by ultrasound assisted sol-gel method and assessed the effect of power, pulse, and solvent quantity. XRD, BET, PSD, and UV-spectrophotometer characterized our samples. We compared the physicochemical properties of the samples obtained with ultrasound-assisted sol-gel and conventional sol-gel process. We also tested their activity by degrading acetaminophen and amoxicillin in a sono-photocatalytic process.

4.2. Materials and methods

4.2.1. Materials

Ti(IV)-butoxide (reagent grade, 97 %), manganese (II) nitrate nonahydrate (reagent grade, 98 %), nitric acid (ACS reagent, 70 %), ethanol (HPLC grade, ≥98 %) Acetaminophen (APAP, analytical standard) and amoxicillin (AMO, analytical standard) were purchased from Sigma Aldrich. We employed all the materials without further purification.

4.2.2. Synthesis

We designed our experiments based on a three operating parameters factorial design: power, pulse, and solvent quantity (Table 4-1). We synthesized Mn-doped TiO_2 catalysts by a modified sol-gel

method assisted by ultrasound. A 500 W ultrasonic processor assisted the synthesis and the degradation of AMO and APAP (VCX 500, Sonics & Materials, Inc.). We equipped the probe with a 20 mm diameter replaceable tip. We calibrated the ultrasonic processor periodically with the method described by Uchida and Kikuchi [35]. We added dropwise the mixture of water and $Mn(NO_3)_2$ (1 mole) to the solution mixture of titanium (IV) butoxide (5 moles), ethanol (100, 50 and 25 moles), and HNO_3 (5 moles) after starting the sonication. The reaction occurred under US irradiation at three different powers (10, 20, 30 W) and pulses (no pulse, 1-1 and 2-2 s on/off) for 3.5 h. Afterward, the gels aged at room temperature for 12 h and dried overnight at 100 °C in an oven under static atmosphere. A furnace calcined the samples at 450 °C for 5 h (Table 4-1). Sample TM20-195-0 and TM30-195-2 calcined at 550 °C for 5 h for studying the effect of calcination temperature (Table 4-1). In order to compare the synthesizing procedure with the conventional sol-gel process, two samples were prepared by the conventional sol-gel method (Table 4-1). The samples aged and dried at 100 °C overnight. Calcination temperatures were 450 °C and 550 °C.

4.2.3. Analytical

A Philips PANanalytical (USA) X'pert diffractometer measured samples' crystallinity at ambient temperature with an angle of incidence of 0.5 ° and Cu Kα (1.5406 Å) radiation at 50 kV and 40 mA. The instrument scanned the diffraction angle between 20° and 80°, with a divergence slit of 1°.

We calculated the anatase, rutile and brookite phase content of the samples according to the Zhang and Banfield equation [36].

An AUTOSORB-1 (Quantachrome Instruments, USA) measured the specific surface area of the samples by the standard multi-point Brunauer–Emmett–Teller (BET). A furnace degassed the samples at 200 °C for 12 h in vacuum. The desorption isotherm determined the pore size distribution according to the Barret–Joyner–Halender (BJH) method with cylindrical pore size.

A laser scattering analyzer (LA-950 Horiba) determined the particle size distribution (PSD) by applying the Mie algorithm with.

A Thermoscientific UV–VIS Evolution 300 spectrophotometer equipped with a diffuse reflectance accessory (Pike technology EasiDiff) calculated the band-gap (*E*) of each sample with Plank's equation [25]. The instrument scanned the samples in the wavelength range of 200 to 900 nm.

A Varian Prostar HPLC-UV instrument (model 210), equipped with a Microsorb MV 100-5 C18 column (250 mm × 4.6 mm, Variant, Agilent Technologies) monitored the conversion of AMO and APAP. Methanol (0.5 mL min^{-1}) was the eluent (HPLC grade, ≥99.9 %). The UV detection wavelength were 275 nm for AMO and 210 nm for APAP.

Table 4-1. Experimental design; factorial design.

Sample name	Power (W)	Solvent (mole)	Pulse (s)	Calcination Temperature (°C)
TM10-49-0	10	49	Continuous US	450
TM10-195-1	10	195	1-1	450
TM10-98-2	10	98	2-2	450
TM20-195-0	20	195	Continuous US	450
TM20-98-1	20	98	1-1	450
TM20-49-2	20	49	2-2	450
TM30-98-0	30	98	Continuous US	450
TM30-49-1	30	49	1-1	450
TM30-195-2	30	195	2-2	450
TM20-195-0-550	20	195	Continuous US	550
TM30-195-2-550	30	195	2-2	550
Sol-gel-450	-	195	No US	450
Sol-gel-550	-	195	No US	550

4.2.4. Sonophotocatalysis tests

We prepared 150 mL solution of 25 ppm of APAP or 100 ppm of AMO in a jacketed glass reactor and applied a continuous sonication (20 W) and UVA radiation (160 Wm^{-2}) for 3h. Cooling water kept the temperature of the solution at 10 °C through all the test. The catalyst concentration was 0.1 g L^{-1}. We sampled the solution every 30 mins for the HPLC analysis.

4.3. Result and discussions

4.3.1. XRD

The XRD patterns of Mn-doped TiO_2 calcined at 450 °C (Figure 4-1) match with anatase (peak at 25.4°) and rutile (peak at 27.4°) (the most intense peaks) phases without any peak for Mn (Mn oxide, metallic Mn), which means that Mn is well dispersed within TiO_2 lattice [37], [38]. 45 % to 56 % of the crystalline phase of TiO_2 is anatase and 14% to 26% is rutile (Table 4-2). The ionic radius and the charge of the dopant alter the structure of TiO_2. If the dopant charge is lower than that of Ti^{4+}, it alters the concentration of oxygen vacancies depending on the position within the TiO_2 matrix; it either replaces Ti in the lattice or occupies an interstitial position depending on its size and concentration. Mn^{2+} has a larger ionic radius (0.8 Å) than Ti (0.68 Å). Therefore, Mn^{2+} ions only replace Ti^{4+} in the lattice sites. The replacement by metal ions with a valence lower than 4+ and higher ionic radius than 0.68 Å induces oxygen vacancies at the boundaries of anatase grains, which favors bond rupture and solid-state ionic rearrangement [30], [39]–[41].

The formation of crystalline phases and their transformation from anatase to rutile depends on the starting material, deposition method and calcination temperature [42]–[44]. Despite rutile is the most stable, anatase is the most active. The combination of anatase and rutile has synergistic effects, compared to the pure phases [45]. In fact, anatase has a larger band gap than rutile. However, the indirect band gap of anatase is smaller than its direct one while in the case of rutile both are similar. Material with indirect bandgap shows longer charge carrier lifetime compared to materials with direct bandgap [45]. Therefore, anatase has longer electron-hole pair life, which makes it more suitable for charge carrier in order to participate in the surface reaction.

This phenomenon transfers an electron from TiO_2 to adsorbed molecules and increases the oxidation power of electrons. On the other hand, the surface properties affect the molecule

adsorption and charge transformation. These properties vary with surface orientation and reconstruction and enhance the surface effects in photocatalytic reactions. Surface properties affect, (i) the adsorption of molecules, (ii) the defects electronic structure, which in turn affects the charge separation and hole-trapping properties, (iii) interaction of molecules with the surface defects, (iv) the surface potential, which influences the charge transfer from the photocatalyst to molecules [41], [44], [46].

Table 4-2. Anatase, rutile, and brookite % of the samples prepared with different conditions with ultrasound and calcined at 450 °C.

Samples	XRD		
	Anatase %	Rutile %	Brookite %
TM10-49-0	56	14	28
TM10-195-1	52	14	34
TM10-98-2	45	20	35
TM20-195-0	48	21	31
TM20-98-1	51	18	31
TM20-49-2	44	22	30
TM30-98-0	47	18	30
TM30-49-1	45	26	28
TM30-195-2	50	16	35

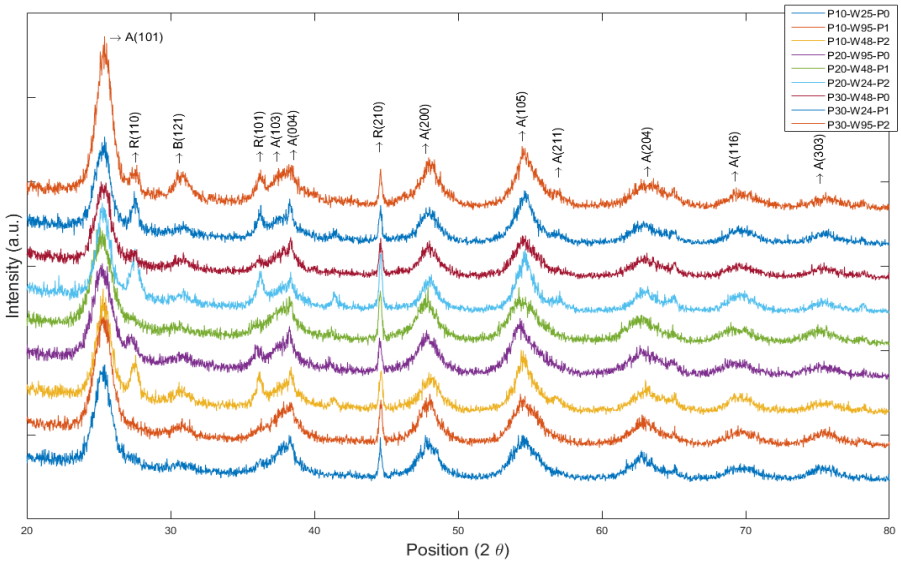

Figure 4-1. XRD pattern of samples prepared with ultrasound and calcined at 450

4.3.2. BET

The N_2 adsorption-desorption patterns of the Mn-doped TiO_2 powders are type IV isotherms (Figure 4-2) with a type H3 hysteresis loop (which indicates that powders contain mesopores from 2 nm to 50 nm). For all the catalysts, the pore size is 2 nm to 3 nm (Table 4-3). The IV isotherm of the catalyst has type E pore shape with a thin-neck-bottle-shape. The pore size decreases because (1) small crystallites aggregate, and (2) Mn ions place inside the pores of TiO_2 [22], [41].

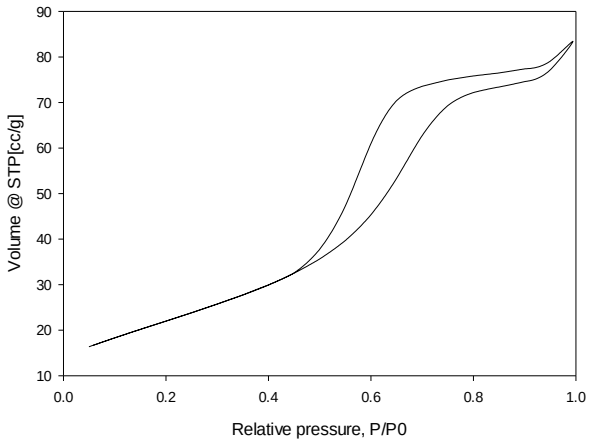

Figure 4-2. Example of N_2 adsorption-desorption isotherm of a Mn-doped TiO_2 powder.

Table 4-3. Average pore size, pore volume, and surface area of the samples prepared with ultrasound and calcined at 450 °C, error within ±1 %.

Samples	BET		
	Average pore size (Å)	Pore volume (cc g^{-1})	Surface area (m^2 g^{-1})
TM10-49-0	19	0.13	101
TM10-195-1	28	0.24	154
TM10-98-2	24	0.13	102
TM20-195-0	24	0.29	158
TM20-98-1	25	0.20	132
TM20-49-2	22	0.14	102
TM30-98-0	28	0.20	121
TM30-49-1	19	0.14	138
TM30-195-2	22	0.25	128

4.3.3. PSD

The Mie theory applies to Mn-doped TiO_2 particles as all the mean particle sizes range between 4 µm and 13 µm and the particle median sizes range between 4 µm and 11 µm (Table 4-4).

Ultrasonic cavitation in comparison to the conventional sol-gel process reduces the particle size, as well as the size of agglomerates on the support. However, the smaller the particles, the higher the susceptive to sintering during calcination [25], [47].

Table 4-4. Median size and mean size of the samples prepared under different sonication conditions and calcined at 450 °C, error within ±2 %.

Samples	PSD	
	Median size (μm)	Mean size (μm)
TM10-49-0	9	10
TM10-195-1	9	10
TM10-98-2	9	10
TM20-195-0	11	13
TM20-98-1	7	8
TM20-49-2	4	4
TM30-98-0	8	9
TM30-49-1	9	10
TM30-195-2	9	10

4.3.4. UV-Vis absorbance and Band-Gap

All samples turned from white to grey upon calcination. The color of the sample depends on the Mn dopant concentration and it darkens as the concentration of dopant increases [26]. UV-Vis measured the absorbance wavelength of the samples of Mn doped TiO_2 (Table 4-5).

The absorbance wavelength of bare TiO_2 has a sharp edge at 400 nm, which is related to the excitation of the electron from the valence band to the conduction band of the semiconductor (Figure 4-3) [25] . Bare TiO_2 absorbs in the ultraviolet region of the spectrum as it has a band gap energy of 3.2 eV. Metal doping red shifts the absorption of TiO_2 depending on the amount of doping content [17], [30], [48]. Moreover, the preparation of nanoparticles with a sonochemical

method promotes the shift of the absorbance wavelength toward the visible region compared to the conventional sol-gel process [18], [49].

The band-gap of all Mn-doped samples ranged from 1.6 eV to 1.91 eV. The shift of the absorption in the visible region ascribes to the broad absorption of transition metals and the effect of doping of pure TiO_2. Mn decreased the band-gap of the catalysts to less than 2 eV.

Samples prepared at 200 W L^{-1} (TM10-195-1, TM20-98-1, TM30-98-0, TM30-58-1, and TM20-58-2) have an absorbance up to 0.95 a.u. compared to the samples prepared at 150 W L^{-1} whose absorbances reach a maximum of 0.85 a.u. The higher the ultrasonic power density, the more turbulent the mixing among the components. At 200 W L^{-1}, the structure of the catalyst is more intercalated, and absorbance increases.

The mentioned samples were prepared with an ultrasonic power density higher than 200 W L^{-1} and therefore the cavitation affects the mixing among the components and structure of the catalysts. However, for the remaining samples, the power density delivered is less than 150 W L^{-1} and their absorbance is lower, up to maximum 0.85 a.u.

Stucchi et al. reported that Mn increases the absorption wavelength of TiO_2 to above 700 nm and provides a band gap energy of 1.59 eV.

Oxygen occupies the 2p and 4d orbitals of the valence band (VB) of TiO_2. DFT calculations reported the existence of oxygen vacancies in TiO_2 without affecting the overall band-gap that induce a donor level next to the mid-gap (deep level) defect states. By shifting the valence band to the lower binding energies, the absorption peak edges shift to the red region. A high concentration of Mn provokes the recombination of electron-hole pairs, which is due to the appeared lattice defects [28].

When Mn^{2+} traps electrons, its electronic configuration changes from $3d^5$ to $3d^6$, and when it traps holes its electronic configuration changes to $3d^4$. Both states are unstable and as a consequence, to restoring its stable configuration, Mn donates the trapped electron to an oxygen molecule and the trapped hole to the water adsorbed onto the surface to generate superoxide (O_2^-) and hydroxyl ($OH^\bullet$) radicals:

$$Mn^{2+} + e^- \rightarrow Mn^+ \quad (4)$$

$$Mn^+ + O_2ads \rightarrow Mn^{2+} + O_2^{\bullet-} \quad (5)$$

$Mn^{2+} + h^{+} \rightarrow Mn^{3+}$ (6)

$Mn^{3+} + OH^{-} \rightarrow Mn^{2+} + OH^{\bullet}$ (7)

The half electronic structure of Mn^{2+} accelerates the charge transfer process and causes it to act as a shallow trap for the charge carriers. Therefore, the generation of highly active oxidative species increases [40].

Table 4-5. Band-gap of the samples prepared with different sonication condition with ultrasound and calcined at 450 °C.

Samples	UV-vis
	Band-gap (eV)
TM10-49-0	1.91
TM10-195-1	1.83
TM10-98-2	1.91
TM20-195-0	1.6
TM20-98-1	1.71
TM20-49-2	1.77
TM30-98-0	1.65
TM30-49-1	1.6
TM30-195-2	1.77

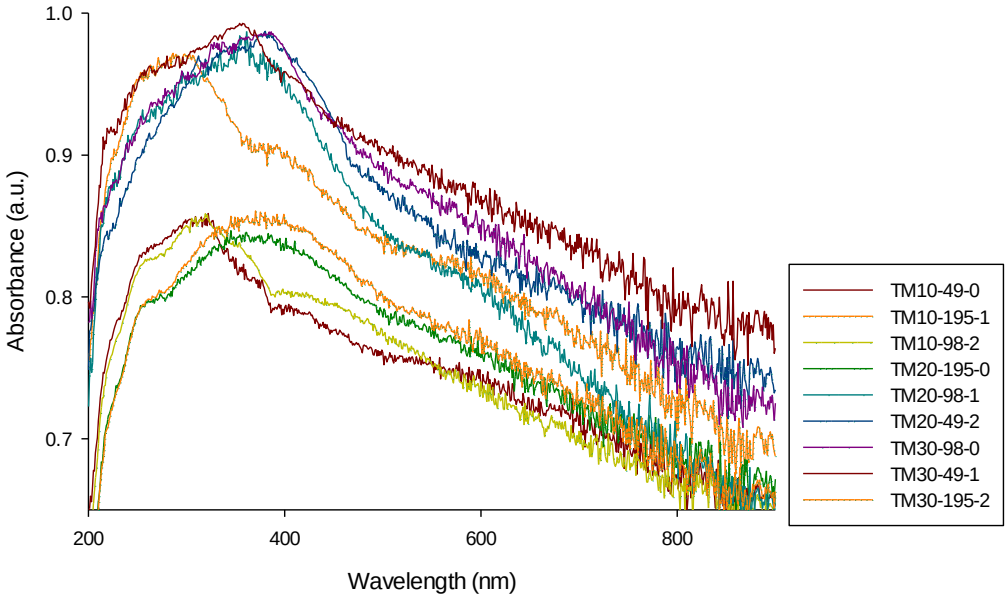

Figure 4-3. Absorbance spectra of Mn-TiO_2 samples

4.3.5. Power effect

At low power [0-16 W], the release of energy inside the solution is not enough for the transformation of anatase to rutile (Figure 4-4 and Figure S-1). The higher the power, the higher the transformation of anatase to rutile phase. By increasing the amplitude, the energy within the hot-spot increases, which is favorable for crystal growth [50]. Despite the high temperature within hot-spots, the cooling rates are in the order of millisecond [51]. At high amplitude i.e. 40 %, ethanol partially vaporizes. This shifts the equilibrium of the system reaction, which results in an increase in the phase transformation from anatase to rutile. At power in the range of 15-20 W, the high temperature balances the high energy collapse, thus limiting the local volatilization. Moreover, dissipated mechanical heat energy will make phase transformation more rapid.

However, during the sonication process, small bubbles close to the horn coalesce and form larger bubbles. Acoustic shielding is the reflection of acoustic energy from large bubbles towards the horn, caused by the large bubbles, being too large to absorb the acoustic energy. Due to this fact, small bubbles cannot absorb significant amounts of energy and it causes an inhomogeneous distribution of energy inside the liquid. At higher amplitude, acoustic shielding increases and leads to the reduction in % rutile [52]. Cavitation depends on power as well. At power lower than 10 W,

stable cavitation occurs whereas above that value cavitation is transient [53]. The higher the power, the higher the number of cavitation bubbles. However, there is not enough time for the accumulation of ethanol at the surface of the bubble/solution and for the evaporation of water and ethanol. Moreover, by increasing the power, the size of the bubbles that are produced at high local temperatures decreases [53].

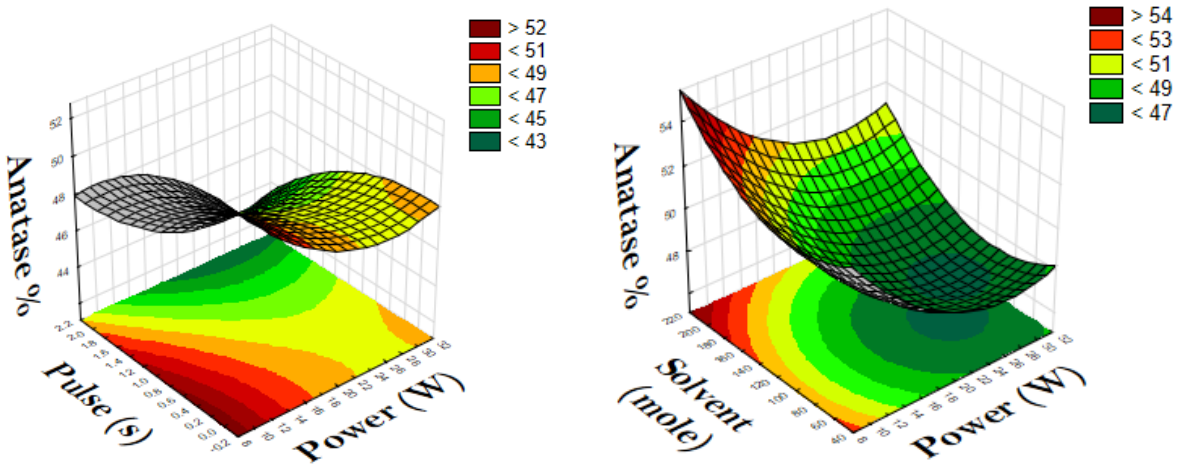

Figure 4-4. Effect of ultrasound power on anatase %

Figure 4-5 and S-2 show the effect of the power on the surface area, pore volume, and average pore size. Corresponding to the graphs it's possible to have an optimum frequency in ultrasound preparation particles. An optimum value results in higher surface area and pore volume and smaller pore size. However, at a lower or higher value than the optimum value of power, surface area and pore volume decrease and pore size increases.

Power density, frequency, and wattage of the system define the characteristics of ultrasound [24]. The power density is one of the influential parameters on TiO_2 properties. A minimum intensity or power is required to achieve cavitation. Under certain conditions, particles continuously form until an optimum value of power/amplitude is reached. High power or amplitude is necessary to achieve enough mechanical vibration to promote cavitation in the sample. However, high power and amplitude cause the deterioration of the transducer, which leads to the agitation of the solution

instead of cavitation, causing poor transmission of ultrasound through the liquid medium. In addition, high power/amplitude causes undesired effects such as degradation of structures. Therefore, a high power disrupts the bubble dynamic as it grows, and this leads to poor cavitation and growth of material [54]. Also, at high power/amplitude the efficiency of removal of deposit increases and there is less chance for crystallization to occur [55]. At higher power/amplitude, cushioning effects decrease, transferring energy to the system and therefore it will give lower cavitation activity [56]. Yu et al. prepared TiO_2 particles with ultrasound, achieving a surface area of 112 m^2 g^{-1}, a pore size of 6.7 nm. They proved that a high amplitude gives particles with higher surface area and pore diameter (around 7 nm) [57].

Figure 4-6 shows the effect of operative parameters on particle size. At an optimum value of power results in smaller particle size while with the power lower or higher than this amount cause formation particles with the larger size. The nucleation process is important to the determination of the particle size. High-velocity collisions among the particles induced by intense shock waves, and thus a neck between particles is formed from localized melting. Generally, the mechanical strength (physical) effects associated with microbubbles are inversely proportional to ultrasound power. At low power, the mechanical effects on the sonochemical nucleation and growth processes of metal clusters and particles are negligible [53]. Greater sonication power forms smaller particles.

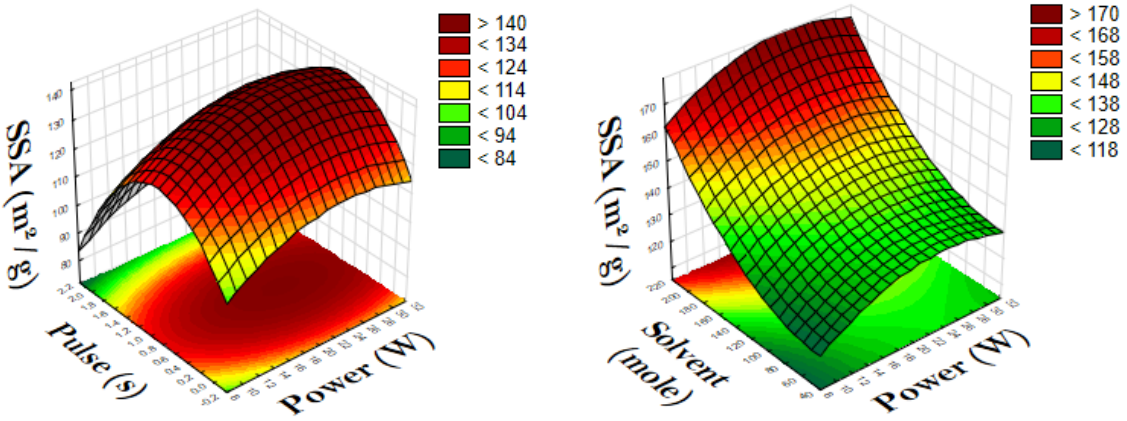

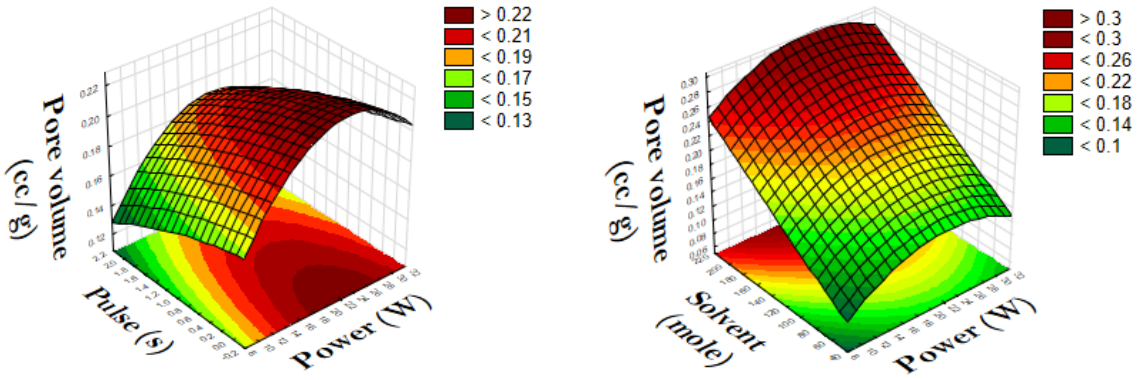

Figure 4-5. Effect of ultrasound power on textural properties

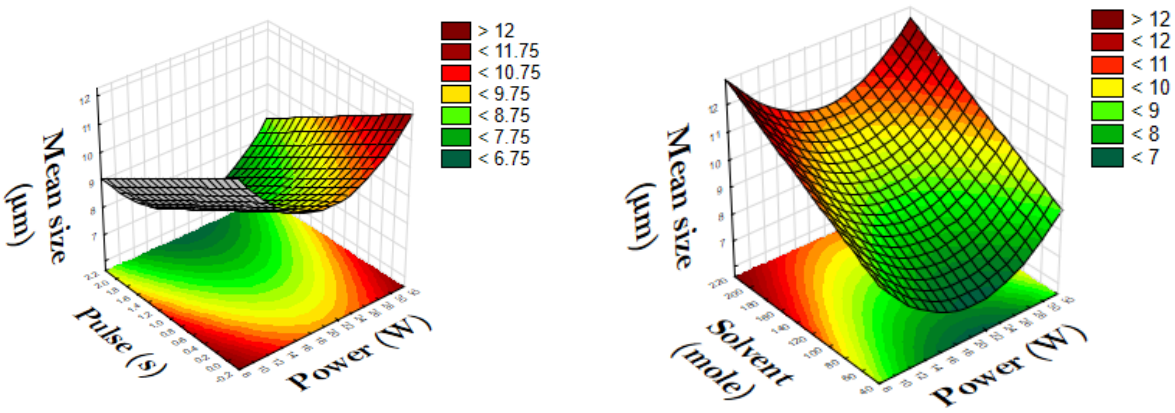

Figure 4-6. Effect of ultrasound power on particle size

Figure 4-7 shows the effect of operating parameters on band-gap. Increasing in the power results in smaller band-gap. However, above certain power (20 W), there is no significant effect on narrowing the band-gap. Cavitation and collapsing of the bubbles induce turbulence inside the liquid and increase the diffusion of materials. Therefore, Mn diffuses more inside TiO_2 lattice and replace instead of Ti ions and as a result, Mn ions well disperse in TiO_2 lattice and decrease the band-gap of the materials. Moreover, by increasing the power the crystallinity increases. By increasing the crystallinity, the bandgap will be narrower. However, after a certain amount of power, it doesn't affect the band-gap.

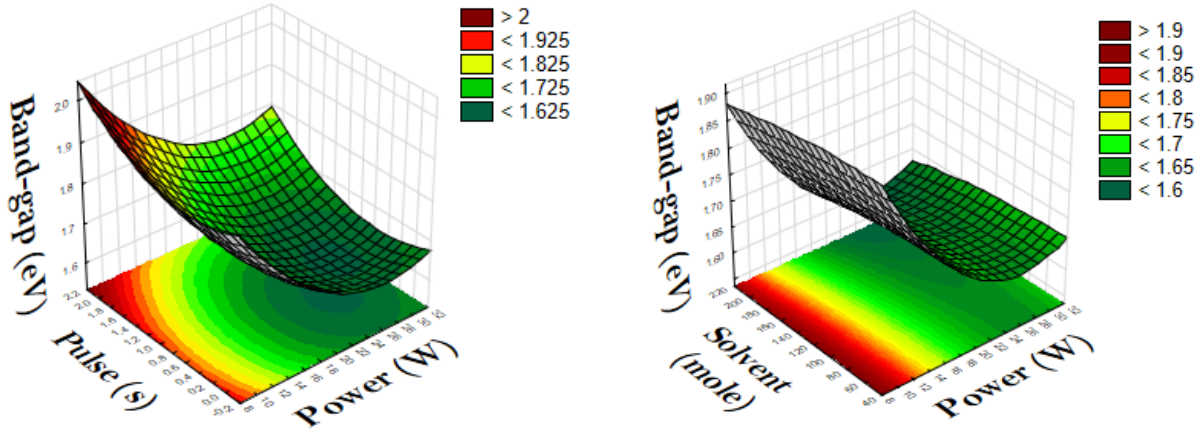

Figure 4-7. Effect of ultrasound power on Band-gap

4.3.6. Pulse effect

In order to reduce the net power consumption in the system and producing interruption to cool down the transducers, we used the pulsed ultrasound (a few seconds on followed by a few seconds off). Pulse has an optimum value (1 s) when it comes to the ultrasonic preparation of nanoparticles (Figures 4-8 to 4-11, S-3, S-4). Pulse sonication produces smaller crystal particles. Especially for high current densities, nucleation occurs at a high rate during each pulse. In shorter pulse sonication, instead, the growth of crystal by the creation of new nuclei, or deposition on the already existing nuclei, is slow. Crystal size may or may not increase with the number of pulses. It depends on whether each new pulse forms a new nucleus or adds to pre-existing ones. If the new nuclei form during each pulse, the crystal size will be smaller [55].

Pulsed ultrasound reduces the net power consumption in the system and allows the transducer to cool down faster. τ_1 and τ_2 are the pulse lengths. τ_1 is the time of sonication to produce and grow gas bubbles, whereas τ_2 is the ultrasound off-time during which bubbles dissolve. Nuclei form and grow within the τ_2 [58]. At short pulse, the ultrasound smoothly stirs the solution and crystallization has less time to occur [55], [56]. On the other hand, at longer pulse sonication times, the number of active bubbles decreases due to the degassing [58]. Therefore, in order to achieve

maximum cavitation efficiency, the optimum pulse sonication must be identified [54]. The minimum band-gap energy was achieved with a pulse in the range of 0.6-1 s.

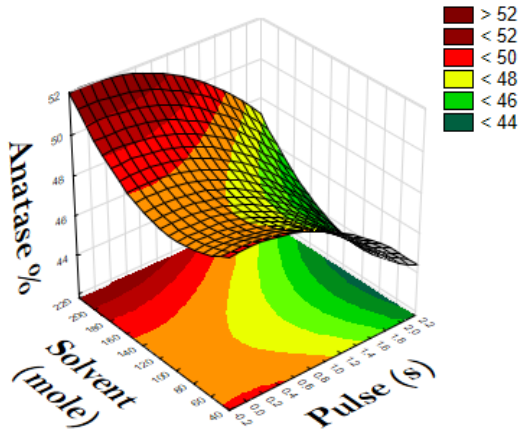

Figure 4-8. Effect of an ultrasound pulse and solvent on Anatase%

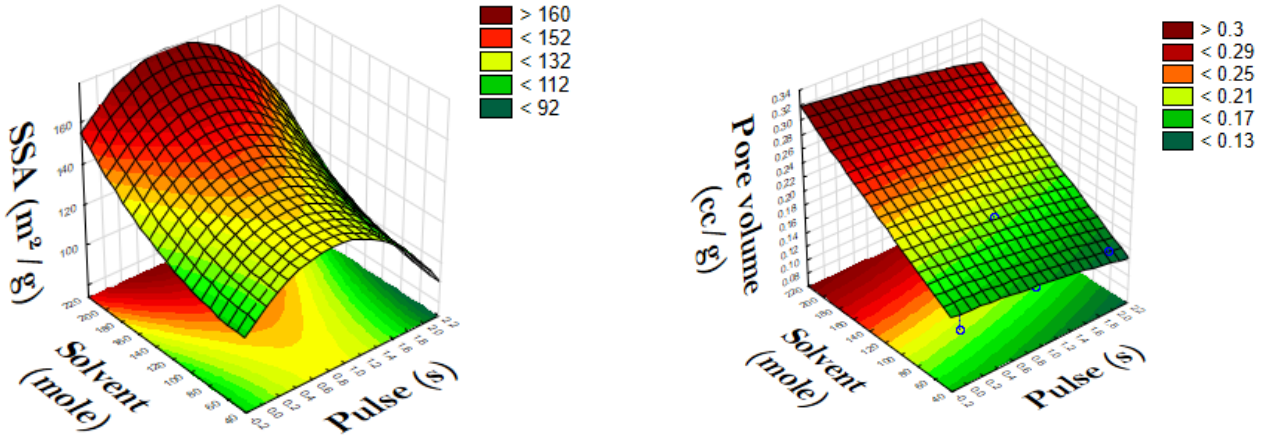

Figure 4-9. Effect of an ultrasound pulse and solvent on textural properties

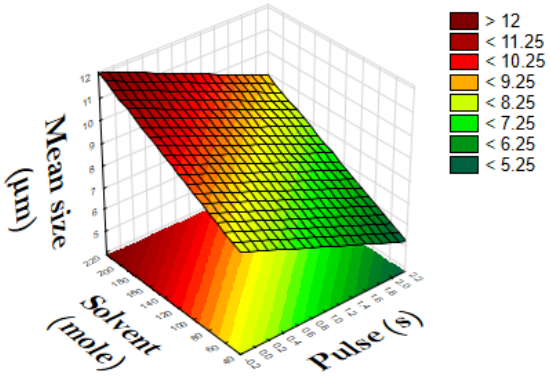

Figure 4-10. Effect of an ultrasound pulse and solvent on particle size

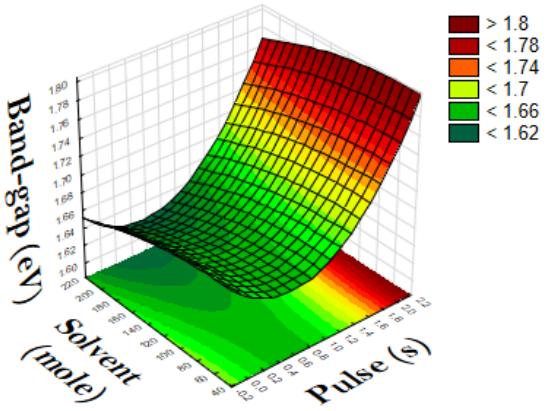

Figure 4-11. Effect of an ultrasound pulse and solvent on Band-gap

4.3.7. Solvent effect

By decreasing the solvent volume, the intensity of the anatase phase decreases (Figure 4-8). This phenomenon ascribes to the fact that ethanol suppresses the hydrolysis of titanium alkoxide and rapid crystallization of TiO_2 particles. Moreover, ethanol is volatile and diffuses into the cavitation bubbles. The ethanol vapor inside the bubble reduces the final temperature in the adiabatic compression. The amount of water during the sol-gel process determines the reaction mechanism and the number of active sites generated [32].

Increasing the amount of solvent results in a homogenous reaction mixture and therefore gives particles with higher surface area and pore volume [17]. In the absence of alcohol, particles present an irregular shape. Alcohol significantly affects the formation of crystals. The growth of crystals occurs by increasing the amount of solvent and it leads to particles with higher surface area and pore volume (Figures from 4-9 to 4-11).

It is well known that water has a significant effect on the creation of the nucleus and the growth of crystals. The higher the amount of water, the more homogeneous the nuclei and the smaller the size of particles. On the other hand, the amount of solvent changes the power density of ultrasound. Decreasing the amount of solvent increase the power density inside the liquid and prevent agglomeration of particles and results in particles with smaller size. However, by increasing the

amount of solvent the power density inside the solution decreases and agglomeration of particles results in larger particles (Figure 4-10).

However, the amount of solvent has no significant effect on the band-gap energy (Figure 4-11).

4.3.8. Photocatalytic degradation

We applied ultrasound and UV irradiation in the presence of Mn-doped TiO_2 powders to the aqueous solution of acetaminophen or amoxicillin for 3 hours. Figure 4-12 and 4-13 show the changes in the concentration of the two molecules of acetaminophen and amoxicillin with different catalysts.

APAP and AMO adsorbed onto the surface of the catalysts with smaller band-gap, higher surface area, and pore volume. The narrower the band-gap of Mn-doped TiO_2 powders, the higher the generation of charge carriers to assist photoelectric reactions and the more enhanced the photoelectric effect [26]. Sample TW20-195-0 with a high surface area of 158 $m^2\ g^{-1}$, a pore volume of 0.29 cc g^{-1}, and mean size of 13 µm and sample TW30-49-1 with a surface area of 138 $m^2\ g^{-1}$, a pore volume of 0.14 cc g^{-1}, and mean size of 10 µm degraded amoxicillin by 52% and 51%, respectively. They degraded AMOX better than other catalyst. These two catalysts have higher absorbance in comparison to other catalyst and therefore they have a higher generation of charge carriers to assist photoelectric reactions. On the other hand, catalyst TW10-98-2 with a low surface area of 102 $m^2\ g^{-1}$, a pore volume of 0.13 cc g^{-1} and mean size of 10 µm has low absorbance compared to other catalyst and therefore it degraded AMOX less than other catalysts (Figure 4-12).

Catalyst TW20-98-1 with a surface area of 132 $m^2\ g^{-1}$, a pore volume of 0.2 cc g^{-1}, and mean size of 8 µm is among the catalyst that absorbs light more than others, therefore in degradation of APAP has the highest removal. Although catalyst TW10-49-0 with a surface area of 101 $m^2\ g^{-1}$, a pore volume of 0.13 cc g^{-1}, and mean size of 10 µm is among the catalyst with lower absorbance. This catalyst has the least degradation of APAP (Figure 4-13).

Acetaminophen and amoxicillin, due to their different molecular properties (such as pKa and polar surface), adsorb differently. Amoxicillin and acetaminophen have a pKa of 2.8 and 9.4, respectively. Amoxicillin is more acidic than acetaminophen and, therefore, it adsorbs better onto

the OH-covered surface of TiO_2. Also, amoxicillin has a polar surface area of 140 $Å^2$ while acetaminophens' is 49 $Å^2$ [25].

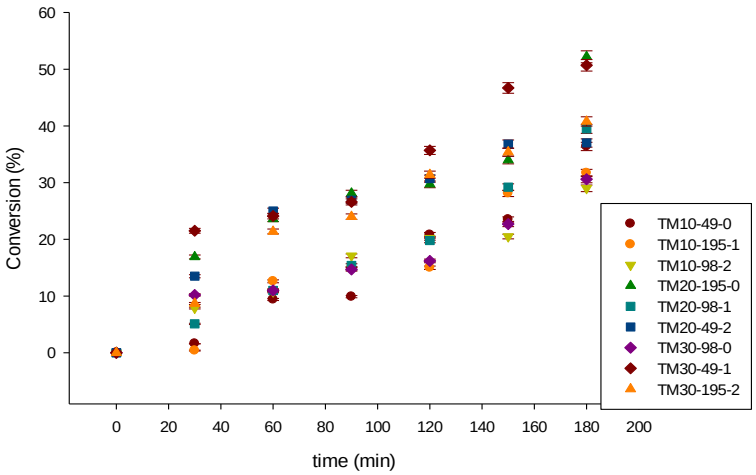

Figure 4-12. Amoxicillin degradation with prepared catalysts, error within ±2%.

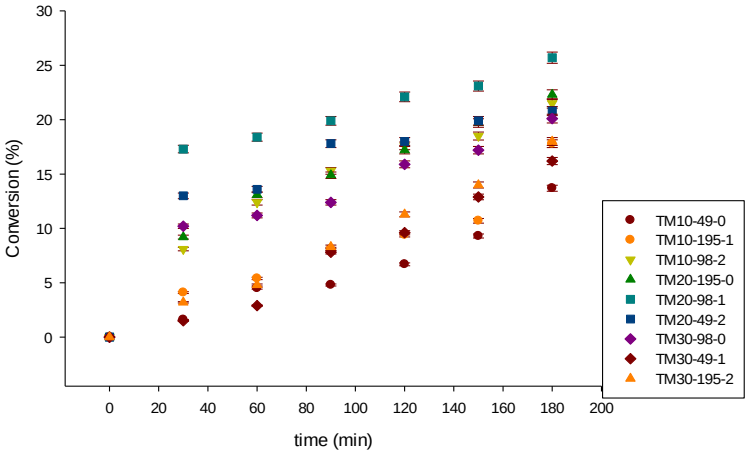

Figure 4-13. Acetaminophen degradation with prepared catalysts, error within ±2%.

4.3.9. Calcination temperature effect

Table 4-6 and figures 4-14 and 4-15 show the effect of the calcination temperature on the band-gap of the samples TM20-195-0 and TM30-195-2. Increasing the temperature from 450 °C to 550

°C, decreased the band gap from 1.77 eV to 1.65 eV for sample TM30-195-2, whereas for sample TM20-195-0 there is a slight increase from 1.6 eV to 1.63 eV. This is due to the fact that crystallinity increased with the increase in the calcination temperature [37].

High calcination temperatures promote crystal growth. Previous studies mentioned that amorphous structure turns to anatase phase at 400 °C and upon increasing temperature anatase becomes rutile (A→R). The primary formed structure of TiO_2 contains defect sites. However, the temperature increase breaks the bonds and elicits atom rearrangement. The increment of temperature causes the coalescence of pores and the total surface area reduces. Also, particles coalescence and their mean particle size increases [37]. Tables 9 and 10 report the effect of the increasing temperature on the total surface area, total pore volume, pore size, and average particle size. The total surface area decreased from 158 $m^2 g^{-1}$ to 90 $m^2 g^{-1}$ and the pore volume decreased from 0.29 cc g^{-1} to 0.25 cc g^{-1} (Table 4-7). The median size and mean size of the sample TM30-195-2 increased from 9 µm and 10 µm at 450 °C, and to 40 µm and 43 µm at 550 °C, respectively (Table 4-8).

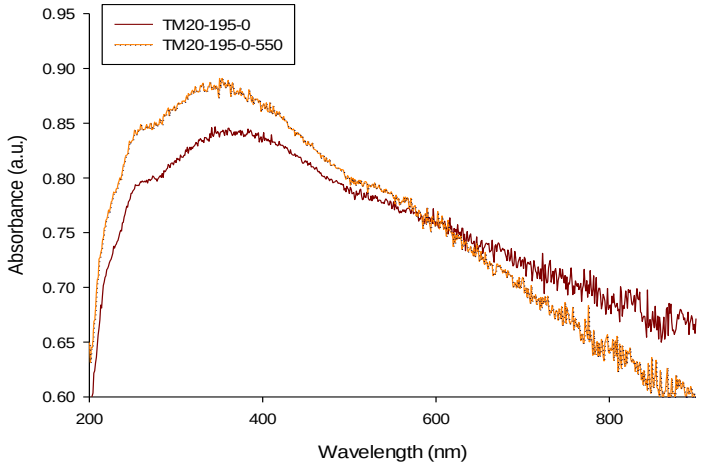

Figure 4-14. Absorbance spectra of Mn-TiO2 samples calcined at 450 °C and 550 °C.

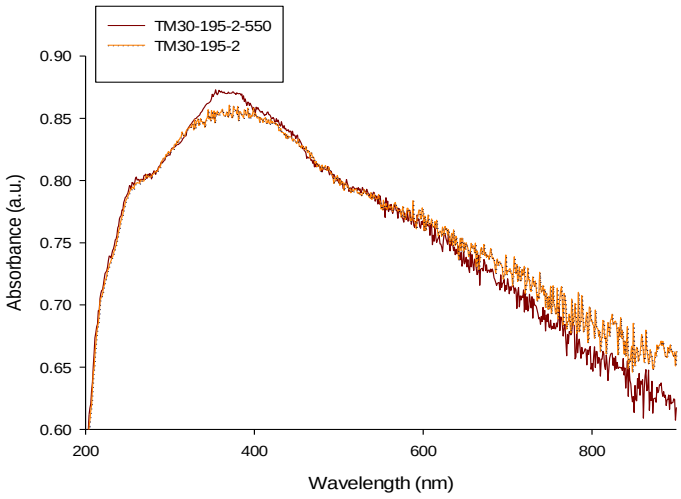

Figure 4-15. Absorbance spectra of Mn-TiO2 samples calcined at 450 °C and 550 °C.

Table 4-6. Band-gap of the samples prepared with different condition with ultrasound and calcined at 450 °C and 550 °C.

Samples	Band-gap
TM20-195-0	1.6
TM20-195-0-550	1.63
TM30-195-2	1.77
TM30-195-2-550	1.65

Table 4-7. Average pore size, pore volume, and surface area of the samples prepared with different condition with ultrasound and calcined at 450 °C and 550 °C, error within ±1 %.

Samples	BET		
	Average pore size (Å)	Pore volume (cc g^{-1})	Surface area (m^2g^{-1})
TM20-195-0	24	0.29	158
TM20-195-0-550	33	0.25	90

Table 4-8. Median size and mean size of the samples prepared with different condition with ultrasound and calcined at 450 °C and 550 °C, error within ±2 %.

Samples	PSD	
	Median size (µm)	Mean size (µm)
TM30-195-2	9	10
TM30-195-2-550	40	43

4.3.10. Sol-gel process comparison with ultrasonication process

We prepared two samples with the conventional sol-gel process. The mixture of the solution stirred at 400 rpm for 3 h 30 mins and then calcined at 450 °C and 550 °C. Figure 4-14 shows the XRD patterns of the two samples. The fractional composition of anatase at both calcination temperatures is much higher than the sample prepared with ultrasound (Table 4-9). It is evident that the ultrasound affects the phase creation and transformation at 450 °C.

The particle size of these samples is much higher than the sample prepared with ultrasound. The particle size of the sample obtained with the conventional sol-gel process is 181 µm while the largest particle obtained with ultrasound is 13 µm.

As previously mentioned, the particle size increased from 155 µm to 161 µm with the increase of the temperature. Moreover, the surface area decreased from 129 to 48 $m^2 g^{-1}$ due to the coalescence of the pores, and the pore volume decreased from 0.21 to 0.14 cc g^{-1}.

Table 4-9. Anatase, rutile, and brookite % of the samples prepared with the sol-gel process

Samples	XRD		
	Phases		
	Anatase %	Rutile %	Brookite %
Sol-gel- 450	86.2	7	6.9
Sol-gel- 550	73.3	20	6.7

Table 4-10. Band-gap of the samples prepared with the sol-gel process and calcined at 450 °C and 550 °C.

Samples	Band-gap
Sol-gel- 450	1.8
Sol-gel- 550	1.72

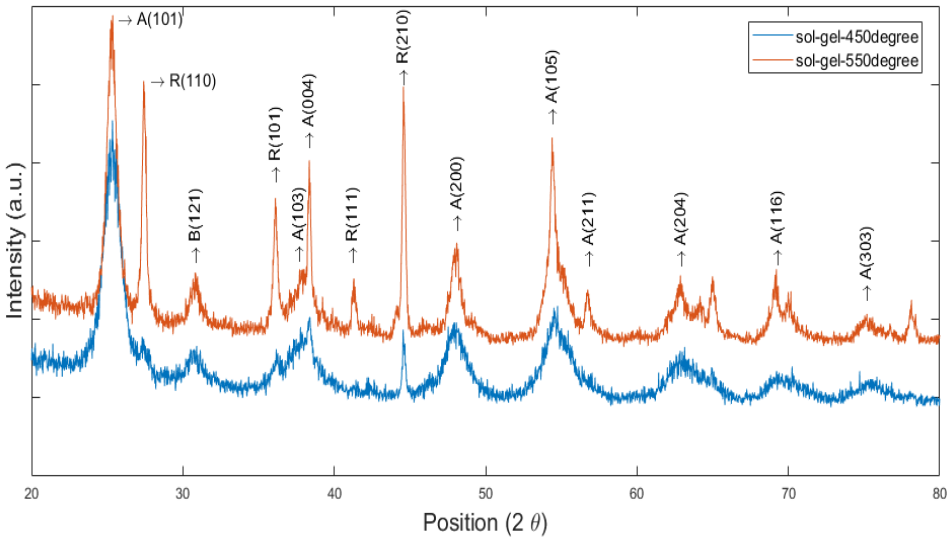

Figure 4-16. XRD pattern of samples prepared with the sol-gel process

Table 4-11. Average pore size, pore volume, and surface area of the samples prepared with the sol-gel process and calcined at 450 °C and 550 °C, error within ±1 %.

Samples	BET		
	Average pore size (Å)	Pore volume (cc g^{-1})	Surface area (m^2g^{-1})
Sol-gel-450	19	0.21	129
Sol-gel-550	33	0.14	48

Table 4-12. Median size and mean size of the samples prepared with the sol-gel process and calcined at 450 °C and 550 °C, error within ±2%.

Samples	PSD	
	Median size (µm)	Mean size (µm)
Sol-gel-450	155	181
Sol-gel-550	160	183

4.4. Conclusion

Doping TiO_2 with Mn increases the light absorption in the visible region due to MnO_x species that absorb in the 390-730 nm range. The ultrasound-assisted synthesis of semiconductors yielded mesoporous Mn-doped TiO_2 powders with a higher surface area (158 m^2 g^{-1}) and pore volume (0.29 cc g^{-1}), and smaller particle size (4 µm) than those obtained with the conventional sol-gel method (181 µm). Power density, pulse, amount of solvent, and calcination temperature elicit specific effects on the final properties of TiO_2 particles. The synthesized catalysts degraded acetaminophen and amoxicillin under UV and ultrasonic irradiation. Amoxicillin decomposed more easily than acetaminophen due to its different molecular properties (such as pKa and polar surface area). The maximum amoxicillin degradation achieved is 52 % with the catalyst with the smallest band-gap (1.6 eV) and the highest surface area (158 m^2 g^{-1}), whereas the maximum acetaminophen degradation was 26 % with the catalyst with the band gap of (1.7 eV) and the surface area of (132 m^2 g^{-1}).

These data open up the route for photocatalytic application under solar light for removing pollutants.

4.5. Acknowledgments

The authors gratefully acknowledge the Fonds de Recherche Nature et Technologie Québec. The authors gratefully acknowledge the support of the Natural Sciences and Engineering Research Council of Canada (NSERC). This research was undertaken, in part, thanks to funding from the Canada Research Chairs program.

References

[1] J. Gomes, R. Costa, R. M. Quinta-Ferreira, and R. C. Martins, “Application of ozonation for pharmaceuticals and personal care products removal from water,” *Sci. Total Environ.*, vol. 586, pp. 265–283, May 2017.

[2] A. M. T. Silva, C. G. Silva, G. Dražić, and J. L. Faria, “Ce-doped TiO2 for photocatalytic degradation of chlorophenol,” *Catal. Today*, vol. 144, no. 1–2, pp. 13–18, Jun. 2009.

[3] Y. Yang, Y. S. Ok, K.-H. Kim, E. E. Kwon, and Y. F. Tsang, “Occurrences and removal of pharmaceuticals and personal care products (PPCPs) in drinking water and water/sewage treatment plants: A review,” *Sci. Total Environ.*, vol. 596–597, pp. 303–320, Oct. 2017.

[4] H. Lu *et al.*, “Fenton-Like Catalysis and Oxidation/Adsorption Performances of Acetaminophen and Arsenic Pollutants in Water on a Multimetal Cu–Zn–Fe-LDH,” *ACS Appl. Mater. Interfaces*, vol. 8, no. 38, pp. 25343–25352, Sep. 2016.

[5] M. B. Ahmed, J. L. Zhou, H. H. Ngo, W. Guo, N. S. Thomaidis, and J. Xu, “Progress in the biological and chemical treatment technologies for emerging contaminant removal from wastewater: A critical review,” *J. Hazard. Mater.*, vol. 323, pp. 274–298, Feb. 2017.

[6] G. Moussavi, Z. Hossaini, and M. Pourakbar, “High-rate adsorption of acetaminophen from the contaminated water onto double-oxidized graphene oxide,” *Chem. Eng. J.*, vol. 287, pp. 665–673, Mar. 2016.

[7] S. S. Sable *et al.*, “Catalytic ozonation of clofibric acid over copper-based catalysts: In situ ATR-IR studies,” *Appl. Catal. B Environ.*, vol. 209, pp. 523–529, Jul. 2017.

[8] “ChemSafetyPro.” [Online]. Available: https://www.chemsafetypro.com.

[9] L. Sellaoui, E. C. Lima, G. L. Dotto, and A. Ben Lamine, “Adsorption of amoxicillin and paracetamol on modified activated carbons: Equilibrium and positional entropy studies,” *J. Mol. Liq.*, vol. 234, pp. 375–381, May 2017.

[10] E. Villaroel, J. Silva-Agredo, C. Petrier, G. Taborda, and R. A. Torres-Palma, “Ultrasonic degradation of acetaminophen in water: Effect of sonochemical parameters and water matrix,” *Ultrason. Sonochem.*, vol. 21, no. 5, pp. 1763–1769, Sep. 2014.

[11] “HealthState.” [Online]. Available: www.health.state.mn.us/cec .

[12] M. Hatat-Fraile *et al.*, “Concurrent photocatalytic and filtration processes using doped TiO2 coated quartz fiber membranes in a photocatalytic membrane reactor,” *Chem. Eng. J.*, vol. 330, pp. 531–540, Dec. 2017.

[13] L. Lin, H. Wang, W. Jiang, A. R. Mkaouar, and P. Xu, “Comparison study on photocatalytic oxidation of pharmaceuticals by TiO2-Fe and TiO2-reduced graphene oxide nanocomposites immobilized on optical fibers,” *J. Hazard. Mater.*, vol. 333, pp. 162–168, Jul. 2017.

[14] E. SELLI, C. BIANCHI, C. PIROLA, G. CAPPELLETTI, and V. RAGAINI, “Efficiency of 1,4-dichlorobenzene degradation in water under photolysis, photocatalysis on TiO2 and sonolysis,” *J. Hazard. Mater.*, vol. 153, no. 3, pp. 1136–1141, May 2008.

[15] M. R. D. Khaki, M. S. Shafeeyan, A. A. A. Raman, and W. M. A. W. Daud, “Application of doped photocatalysts for organic pollutant degradation - A review,” *J. Environ. Manage.*, vol. 198, pp. 78–94, Aug. 2017.

[16] D. Schieppati, F. Galli, M.-L. Peyot, V. Yargeau, C. L. Bianchi, and D. C. Boffito, “An ultrasound-assisted photocatalytic treatment to remove an herbicidal pollutant from wastewaters,” *Ultrason. Sonochem.*, vol. 54, pp. 302–310, Jun. 2019.

[17] R. Ambati and P. R. Gogate, “Ultrasound assisted synthesis of iron doped TiO2 catalyst,” *Ultrason. Sonochem.*, vol. 40, pp. 91–100, Jan. 2018.

[18] R. A. Aziz, N. M. Yusof, and A. K. Masrom, “Effect of Ultrasonic Irradiation Time and Amplitude Variation on TiO2 Particles,” *Solid State Sci. Technol.*, vol. 19, no. 2, pp. 371–383, 2011.

[19] H. Li, G. Liu, S. Chen, and Q. Liu, “Novel Fe doped mesoporous TiO2 microspheres: Ultrasonic–hydrothermal synthesis, characterization, and photocatalytic properties,” *Phys. E Low-dimensional Syst. Nanostructures*, vol. 42, no. 6, pp. 1844–1849, Apr. 2010.

[20] Y. Xie and C. Yuan, “Visible-light responsive cerium ion modified titania sol and nanocrystallites for X-3B dye photodegradation,” *Appl. Catal. B Environ.*, vol. 46, no. 2, pp. 251–259, Nov. 2003.

[21] J. Gomes *et al.*, “Environmental preservation of emerging parabens contamination: effect of Ag and Pt loading over the catalytic efficiency of TiO 2 during photocatalytic ozonation,” *Energy Procedia*, vol. 136, pp. 270–276, Oct. 2017.

[22] L. Song, C. Chen, and S. Zhang, “Sonocatalytic performance of Tb7O12/TiO2 composite under ultrasonic irradiation,” *Ultrason. Sonochem.*, vol. 18, no. 3, pp. 713–717, May 2011.

[23] H. Khan, M. G. Rigamonti, G. S. Patience, and D. C. Boffito, “Spray dried TiO2/WO3 heterostructure for photocatalytic applications with residual activity in the dark,” *Appl. Catal. B Environ.*, vol. 226, pp. 311–323, Jun. 2018.

[24] M. Stucchi *et al.*, “Ultrasound assisted synthesis of Ag-decorated TiO2 active in visible light,” *Ultrason. Sonochem.*, vol. 40, pp. 282–288, Jan. 2018.

[25] M. Stucchi, A. Elfiad, M. Rigamonti, H. Khan, and D. C. Boffito, “Water treatment: Mn-TiO 2 synthesized by ultrasound with increased aromatics adsorption,” *Ultrason. Sonochem.*, vol. 44, pp. 272–279, Jun. 2018.

[26] Q. R. Deng, X. H. Xia, M. L. Guo, Y. Gao, and G. Shao, “Mn-doped TiO2 nanopowders with remarkable visible light photocatalytic activity,” *Mater. Lett.*, vol. 65, no. 13, pp. 2051–2054, Jul. 2011.

[27] V. D. Binas, K. Sambani, T. Maggos, A. Katsanaki, and G. Kiriakidis, “Synthesis and photocatalytic activity of Mn-doped TiO2 nanostructured powders under UV and visible light,” *Appl. Catal. B Environ.*, vol. 113–114, pp. 79–86, Feb. 2012.

[28] L. Wang, X. Zhang, P. Zhang, Z. Cao, and J. Hu, “Photoelectric conversion performances of Mn doped TiO2 under >420nm visible light irradiation,” *J. Saudi Chem. Soc.*, vol. 19, no. 5, pp. 595–601, Sep. 2015.

[29] R. Chauhan, A. Kumar, and R. P. Chaudhary, “Structural and photocatalytic studies of Mn doped TiO2 nanoparticles,” *Spectrochim. Acta Part A Mol. Biomol. Spectrosc.*, vol. 98, pp. 256–264, Dec. 2012.

[30] V. Moradi, M. B. G. Jun, A. Blackburn, and R. A. Herring, “Significant improvement in visible light photocatalytic activity of Fe doped TiO2 using an acid treatment process,” *Appl. Surf. Sci.*, vol. 427, pp. 791–799, Jan. 2018.

[31] K. Prasad, D. V. Pinjari, A. B. Pandit, and S. T. Mhaske, “Synthesis of zirconium dioxide by ultrasound assisted precipitation: Effect of calcination temperature,” *Ultrason. Sonochem.*, vol. 18, no. 5, pp. 1128–1137, Sep. 2011.

[32] N. Ghows and M. H. Entezari, “Ultrasound with low intensity assisted the synthesis of nanocrystalline TiO2 without calcination,” *Ultrason. Sonochem.*, vol. 17, no. 5, pp. 878–883, Jun. 2010.

[33] M. Stucchi, G. Cerrato, and C. L. Bianchi, “Ultrasound to improve both synthesis and pollutants degradation based on metal nanoparticles supported on TiO2,” *Ultrason. Sonochem.*, vol. 51, pp. 462–468, Mar. 2019.

[34] B. Neppolian, Q. Wang, H. Jung, and H. Choi, “Ultrasonic-assisted sol-gel method of preparation of TiO2 nano-particles: Characterization, properties and 4-chlorophenol removal application,” *Ultrason. Sonochem.*, vol. 15, no. 4, pp. 649–658, Apr. 2008.

[35] T. Kikuchi and T. Uchida, “Calorimetric method for measuring high ultrasonic power using water as a heating material,” in *Journal of Physics: Conference Series*, 2011.

[36] H. Khan and D. Berk, “Synthesis, physicochemical properties and visible light photocatalytic studies of molybdenum, iron and vanadium doped titanium dioxide,” *React. Kinet. Mech. Catal.*, vol. 111, no. 1, pp.]3–414, Feb. 2014.

[37] K. Prasad, D. V. Pinjari, A. B. Pandit, and S. T. Mhaske, “Phase transformation of nanostructured titanium dioxide from anatase-to-rutile via combined ultrasound assisted sol–gel technique,” *Ultrason. Sonochem.*, vol. 17, no. 2, pp. 409–415, Feb. 2010.

[38] T. Thirugnanasambandan and M. Alagar, “Titanium dioxide (TiO2) Nanoparticles XRD Analyses: An Insight,” *arXiv*, 2013.

[39] Y. Xu, H. Chen, Z. Zeng, and B. Lei, “Investigation on mechanism of photocatalytic activity enhancement of nanometer cerium-doped titania,” *Appl. Surf. Sci.*, vol. 252, no. 24, pp. 8565–8570, Oct. 2006.

[40] V. C. Papadimitriou *et al.*, “Determination of photo-catalytic activity of un-doped and Mn-doped TiO2 anatase powders on acetaldehyde under UV and visible light,” *Thin Solid Films*, vol. 520, no. 4, pp. 1195–1201, Dec. 2011.

[41] M. Zhou, J. Yu, and B. Cheng, “Effects of Fe-doping on the photocatalytic activity of mesoporous TiO2 powders prepared by an ultrasonic method,” *J. Hazard. Mater.*, vol. 137, no. 3, pp. 1838–1847, Oct. 2006.

[42] A. S. Bakri *et al.*, “Effect of annealing temperature of titanium dioxide thin films on structural and electrical properties,” 2017, p. 030030.

[43] K. Thamaphat, P. Limsuwan, and B. Ngotawornchai, “Phase Characterization of TiO2 Powder by XRD and TEM,” *Kasetsart J. (Nature Sci.*, 2008.

[44] E. M. Mahdi, M. H. Abdul Shukor, M. S. Meor Yusoff, and P. Wilfred, “XRD and EDXRF Analysis of Anatase Nano-TiO_2 Synthesized from Mineral Precursors,” *Adv. Mater. Res.*, 2012.

[45] T. Luttrell, S. Halpegamage, J. Tao, A. Kramer, E. Sutter, and M. Batzill, “Why is anatase a better photocatalyst than rutile? - Model studies on epitaxial TiO2 films,” *Sci. Rep.*, vol. 4, no. 1, p. 4043, May 2015.

[46] G. Glaspell and A. Manivannan, “Sol-gel synthesis and magnetic studies of titanium dioxide doped with 10% M (M = Fe, Mn and Ni),” *J. Clust. Sci.*, 2005.

[47] M. Charghand, M. Haghighi, and S. Aghamohammadi, “The beneficial use of ultrasound in synthesis of nanostructured Ce-doped SAPO-34 used in methanol conversion to light olefins,” *Ultrason. Sonochem.*, 2014.

[48] B. Singaram, K. Varadharajan, J. Jeyaram, R. Rajendran, and V. Jayavel, “Preparation of cerium and sulfur codoped TiO2 nanoparticles based photocatalytic activity with enhanced visible light,” *J. Photochem. Photobiol. A Chem.*, vol. 349, pp. 91–99, Dec. 2017.

[49] S. R. Shirsath, D. V. Pinjari, P. R. Gogate, S. H. Sonawane, and A. B. Pandit, “Ultrasound assisted synthesis of doped TiO2 nano-particles: Characterization and comparison of effectiveness for photocatalytic oxidation of dyestuff effluent,” *Ultrason. Sonochem.*, vol. 20, no. 1, pp. 277–286, Jan. 2013.

[50] J. Yu, M. Zhou, B. Cheng, H. Yu, and X. Zhao, “Ultrasonic preparation of mesoporous titanium dioxide nanocrystalline photocatalysts and evaluation of photocatalytic activity,” *J. Mol. Catal. A Chem.*, 2005.

[51] A. Behzadnia, M. Montazer, and M. M. Rad, “Simultaneous sonosynthesis and sonofabrication of N-doped ZnO/TiO 2 core–shell nanocomposite on wool fabric: Introducing various properties specially nano photo bleaching,” *Ultrason. Sonochem.*, vol. 27, pp. 10–21, Nov. 2015.

[52] J. C. Yu, J. Yu, W. Ho, and L. Zhang, “Preparation of highly photocatalytic active nano-sized TiO2 particles via ultrasonic irradiation,” *Chem. Commun.*, no. 19, pp. 1942–1943, 2001.

[53] K. Okitsu, M. Ashokkumar, and F. Grieser, “Sonochemical synthesis of gold nanoparticles: Effects of ultrasound frequency,” *J. Phys. Chem. B,* 2005.

[54] C. U. Okoli *et al.*, “Solvent effect in sonochemical synthesis of metal-alloy nanoparticles for use as electrocatalysts,” *Ultrason. Sonochem.,* 2018.

[55] Y. Mastai, R. Polsky, Y. Koltypin, A. Gedanken, and G. Hodes, “Pulsed sonoelectrochemical synthesis of cadmium selenide nanoparticles,” *J. Am. Chem. Soc.,* 1999.

[56] S. M. Hingu, P. R. Gogate, and V. K. Rathod, “Synthesis of biodiesel from waste cooking oil using sonochemical reactors,” *Ultrason. Sonochem.,* 2010.

[57] J. C. Yu, L. Zhang, and J. Yu, “Direct sonochemical preparation and characterization of highly active mesoporous TiO2 with a bicrystalline framework,” *Chem. Mater.,* 2002.

[58] D. C. Boffito *et al.*, “Ultrasonic enhancement of the acidity, surface area and free fatty acids esterification catalytic activity of sulphated ZrO2-TiO2 systems,” *J. Catal.,* 2013.

4.6. Supporting result

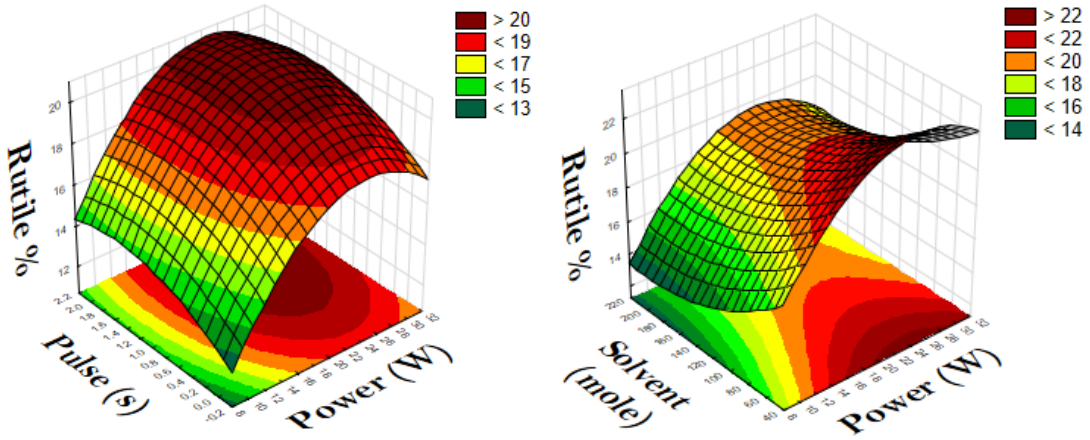

Figure S-1. Effect of ultrasound power on anatase %

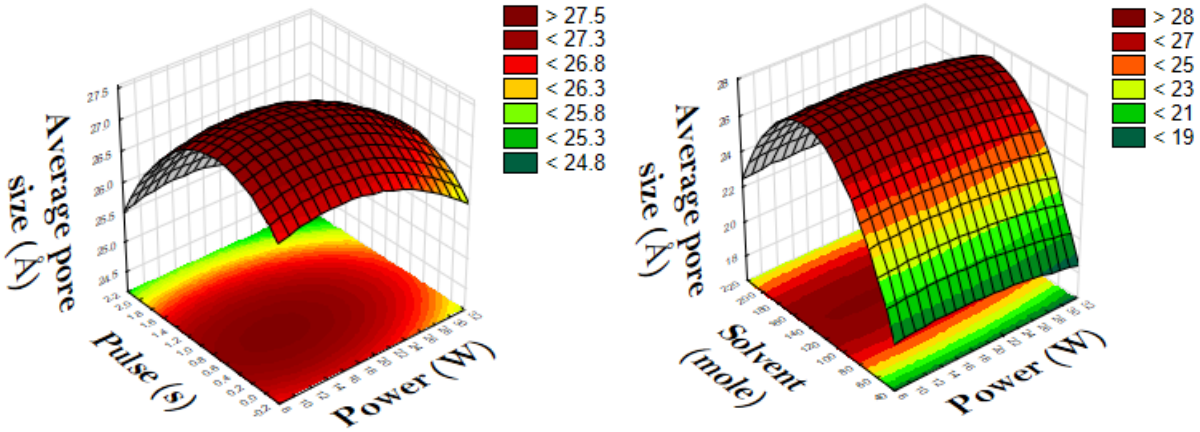

Figure S-2. Effect of ultrasound power on pore size

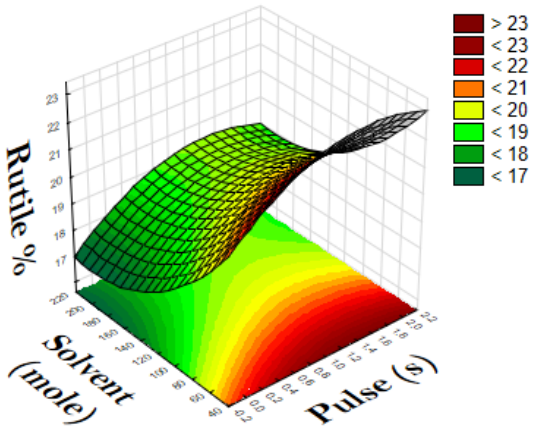

Figure S-3. Effect of an ultrasound pulse and solvent on rutile%

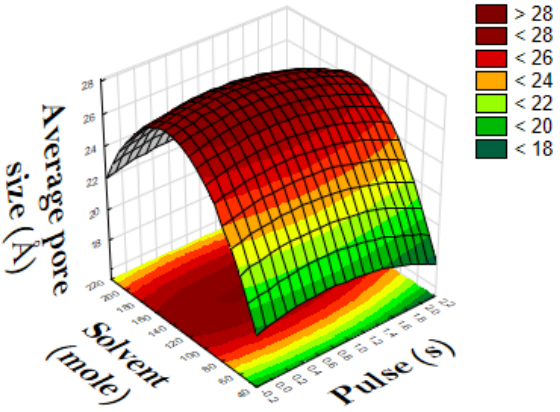

Figure S-4. Effect of an ultrasound pulse and solvent on pore size

CHAPTER 5 GENERAL DISCUSSION

Wastewaters include waters originated from domestic, industrial or agricultural activities. They contain a wide variety of physical, chemical and biological pollutants. Human activity and industrial discharges enormously contribute to the release of pollutants in water, which in turn alter the water cycle thus affecting wildlife and human health. Since conventional physical and biological wastewater treatment can remove a noteworthy amount of these contaminants, scientists are studying new viable methods to increase the efficiency of the pollutant's removal [61-63].

Advanced oxidation processes include photocatalytic, Fenton process, ozonation, and sonolysis, which are the most powerful technologies to oxidize and mineralize organics to carbon dioxide and water as they generate hydroxyl radicals in situ. These processes feature higher efficiency to treat wastewater when combined rather than as individual processes [62]. Ultrasonication is one of the AOPs that delivers ultrasonic waves that cause a rapid collapse of the bubbles and generate hot spots of extreme condition of temperature and pressure. Such conditions lead to hydroxy radicals $OH^{\bullet}$ and other reactive oxidizing species and therefore oxidize organic pollutant in water. Although ultrasonic irradiation alone is not effective to degrade pollutants when it combines with photocatalytic processes, the degradation efficiency increases [63].

In photocatalysis, light irradiates semiconductors and generates unselective reactive oxidizing species with high oxidative power. Titanium dioxide (TiO_2) is the most common semiconductor. It is chemically stable, inexpensive, non-toxic, eco-friendly, and abundant. However, its large band-gap (3.2 eV) and quick recombination of the photogenerated electron-hole pairs limit its application. One of the attempts to modify the TiO_2 performance is to dope TiO_2 with narrow bandgap materials [25]. Noble metals like Ag, Pt, Au, and Pd, and less expensive material of transition metals are the most applied dopant for TiO_2. These materials reduce the bandgap and lower the chances of electron-hole recombination [64].

Among all the catalyst preparation methods, ultrasound has the potential to impact on every stage of catalyst preparation. Ultrasound improves the distribution of the active phase on support and increases nucleation production rate upon the generation of shock waves [24].

The aim of this work was to assess whether ultrasonic cavitation reduces the band-gap energy of Mn-doped TiO_2 under visible light. We studied the effect of operating parameters including power (amplitude), pulse, amount of solvent (mole), and calcination temperature on the properties of the catalysts. Moreover, we synthesized two catalysts with the conventional sol-gel method in order to compare the two synthetic procedures. Ultrasonic cavitation reduced the band-gap from 3.2 eV to 1.6 eV and shifted the absorbance wavelength to the visible region of the electromagnetic spectrum. All the operative parameters affected the Mn-doped TiO_2 properties. Ultrasound-assisted sol-gel synthesis yielded powders with a smaller particle size (below 12 μm), higher surface area (above 120 m^2 g-1) and pore volume (above 0.25 cc g-1) than the conventional method. The activity of catalysts was assessed by degrading acetaminophen and amoxicillin in water.

CHAPTER 6 CONCLUSION AND RECOMMENDATIONS

Doping TiO_2 with Mn increases the light absorption due to the existence of MnO_x species that absorb in the visible light. Synthesizing semiconductors with ultrasound produced mesoporous Mn-doped TiO_2 powders with increased surface area and porosity, and decreased particles size. Samples prepared by ultrasound possessed smaller particle sizes and higher surface area in comparison to the sample prepared by the conventional sol-gel process. Power density, pulse, water: ethanol mole ratio, and calcination temperature specifically control the properties of TiO_2 particles. The Mn-doped TiO_2 catalysts prepared degraded acetaminophen and amoxicillin under ultraviolet and ultrasound irradiation. Amoxicillin oxidized more easily than acetaminophen due to its different molecular properties (such as pKa and polar surface area). The maximum amoxicillin degradation was 52 % with the catalyst with the smallest band-gap (1.6 eV) and the highest surface area (158 $m^2\ g^{-1}$). The maximum acetaminophen degradation was 26 % with the catalyst with the bandgap of 1.7 eV and the surface area of 132 $m^2\ g^{-1}$.

In the present project, we optimized four operative parameters. However, the amount of metal dopant, sonication time, stirring are the other parameters that affect the catalyst properties. The first recommendation for future work is to optimize such parameters.

Moreover, for the degradation of APAP and AMO, we applied ultrasound and ultraviolet irradiation at fixed values. Therefore, it would be of interest to assess how the ultrasound power intensity and amplitude affect the degradation of APAP and AMO in water under UV radiation and LED light.

BIBLIOGRAPHY

[1] Lu, H., Zhu, Z., Zhang, H., Zhu, J., Qiu, Y., Zhu, L., & Küppers, S., *Fenton-Like Catalysis and Oxidation/Adsorption Performances of Acetaminophen and Arsenic Pollutants in Water on a Multimetal Cu–Zn–Fe-LDH.* ACS applied materials & interfaces, 2016, **8**(38): P. 25343-25352.

[2] Saucier, C., Karthickeyan, P., Ranjithkumar, V., Lima, E. C., Dos Reis, G. S., & de Brum, I. A., *Efficient removal of amoxicillin and paracetamol from aqueous solutions using magnetic activated carbon.* Environmental Science and Pollution Research, 2017, **24**(6): P. 5918-5932.

[3] Le, T. X. H., Van Nguyen, T., Yacouba, Z. A., Zoungrana, L., Avril, F., Nguyen, D. L., ... & Lacour, S., *Correlation between degradation pathway and toxicity of acetaminophen and its by-products by using the electro-Fenton process in aqueous media*. Chemosphere, 2017, **172**: P. 1-9.

[4] Hatat-Fraile, M., Liang, R., Arlos, M. J., He, R. X., Peng, P., Servos, M. R., & Zhou, Y. N., *Concurrent photocatalytic and filtration processes using doped TiO2 coated quartz fiber membranes in a photocatalytic membrane reactor*. Chemical Engineering Journal, 2017, **330:** P. 531-540.

[5] Villaroel, E., Silva-Agredo, J., Petrier, C., Taborda, G., & Torres-Palma, R. A., *Ultrasonic degradation of acetaminophen in water: Effect of sonochemical parameters and water matrix. Ultrasonics sonochemistry*, 2014, **21**(5): P. 1763-1769.

[6] Ahmed, M. B., Zhou, J. L., Ngo, H. H., Guo, W., Thomaidis, N. S., & Xu, J., *Progress in the biological and chemical treatment technologies for emerging contaminant removal from wastewater: a critical review*. Journal of hazardous materials, 2017, **323**: P. 274-298.

[7] Lin, L., Wang, H., Jiang, W., Mkaouar, A. R., & Xu, P., *Comparison study on photocatalytic oxidation of pharmaceuticals by TiO2-Fe and TiO2-reduced graphene oxide nanocomposites immobilized on optical fibers.* Journal of hazardous materials, 2017, **333**: P. 162-168.

[8] Khaki, M. R. D., Shafeeyan, M. S., Raman, A. A. A., & Daud, W. M. A. W., *Application of doped photocatalysts for organic pollutant degradation-A review*. Journal of environmental management, 2017, **198**: P. 78-94.

[9] Stucchi, M., Elfiad, A., Rigamonti, M., Khan, H., & Boffito, D. C., *Water treatment: Mn-TiO2 synthesized by ultrasound with increased aromatics adsorption*. Ultrasonics sonochemistry, 2018, 44: p. 272-279.

[10] Deng, Q. R., Xia, X. H., Guo, M. L., Gao, Y., & Shao, G., *Mn-doped TiO2 nanopowders with remarkable visible light photocatalytic activity.* Materials Letters, 2011, **65**(13): P. 2051-2054.

[11] Jimmy, C. Y., Yu, J., Ho, W., & Zhang, L., *Preparation of highly photocatalytic active nano-sized TiO2 particles via ultrasonic irradiation.* Chemical Communications, 2001, **19**: P. 1942-1943.

[12] Prasad, K., Pinjari, D. V., Pandit, A. B., & Mhaske, S. T., *Synthesis of zirconium dioxide by ultrasound assisted precipitation: effect of calcination temperature.* Ultrasonics sonochemistry, 2011, **18**(5): P. 1128-1137.

[13] Shirsath, S. R., Pinjari, D. V., Gogate, P. R., Sonawane, S. H., & Pandit, A. B., *Ultrasound assisted synthesis of doped TiO2 nano-particles: characterization and comparison of effectiveness for photocatalytic oxidation of dyestuff effluent*. Ultrasonics sonochemistry, 2013, **20**(1): P. 277-286.

[14] Ghows, N., & Entezari, M. H., *Ultrasound with low intensity assisted the synthesis of nanocrystalline TiO2 without calcination. Ultrasonics sonochemistry*, 2010, **17**(5): P. 878-883.

[15] Mirzazadeh, H., & Lashanizadegan, M., *Improving the catalytic activity of magnetic Fe3O4/ZnO-CdO/reduced graphene oxide for ultrasonic degradation of the organic pollutants and the green oxidation of olefins.* Solid State Sciences, 2018, **79**: P. 48-57.

[16] Su, C., Hong, B. Y., & Tseng, C. M., *Sol–gel preparation and photocatalysis of titanium dioxide*. Catalysis Today, 2004, **96**(3): P. 119-126.

[17] Zhou, M., Yu, J., Cheng, B., & Yu, H., *Preparation and photocatalytic activity of Fe-doped mesoporous titanium dioxide nanocrystalline photocatalysts*. Materials Chemistry and Physics, 2005, **93**(1): P. 159-163.

[18] Choi, J., Cui, M., Lee, Y., Kim, J., Yoon, Y., Jang, M., & Khim, J., *Synthesis, characterization and sonocatalytic applications of nano-structured carbon based TiO2 catalysts*. Ultrasonics sonochemistry, 2018, **43**: P. 193-200.

[19] Huang, W., Tang, X., Wang, Y., Koltypin, Y., & Gedanken, A., *Selective synthesis of anatase and rutile via ultrasound irradiation*. Chemical Communications, 2000, **15**: P. 1415-1416.

[20] Ambati, R., & Gogate, P. R., *Ultrasound assisted synthesis of iron doped TiO2 catalyst.* Ultrasonics sonochemistry, 2018, **40**: P. 91-100.

[21] Chauhan, R., Kumar, A., & Chaudhary, R. P., *Structural and photocatalytic studies of Mn doped TiO2 nanoparticles*. *Spectrochimica Acta* Part A: Molecular and Biomolecular Spectroscopy, 2012, 98: P. 256-264.

[22] Nair, A. K., & JagadeeshBabu, P. E., *Ag-TiO2 nanosheet embedded photocatalytic membrane for solar water treatment.* Journal of Environmental Chemical Engineering, 2017, **5**(4): P. 4128-4133.

[23] Xie, Y., & Yuan, C., *Visible-light responsive cerium ion modified titania sol and nanocrystallites for X-3B dye photodegradation.* Applied Catalysis B: Environmental, 2003, **46**(2): P. 251-259.

[24] Shi, Z., Lai, H., Yao, S., & Wang, S., *Photocatalytic Activity of Fe and Ce Co-doped Mesoporous TiO2 Catalyst under UV and Visible Light*. Journal of the Chinese Chemical Society, 2012, **59**(5): P. 614-620.

[25] Gomes, J., Lopes, A., Bednarczyk, K., Gmurek, M., Stelmachowski, M., Zaleska-Medynska, A., ... & Martins, R. C., *Environmental preservation of emerging parabens contamination: effect of Ag and Pt loading over the catalytic efficiency of TiO2 during photocatalytic ozonation.* Energy Procedia, 2017, **136**: P. 270-276.

[26] Singaram, B., Varadharajan, K., Jeyaram, J., Rajendran, R., & Jayavel, V., *Preparation of cerium and sulfur codoped TiO2 nanoparticles based photocatalytic activity with enhanced visible light*. Journal of Photochemistry and Photobiology A: Chemistry, 2017, **349**: P. 91-99.

[27] Song, L., Chen, C., & Zhang, S., *Sonocatalytic performance of Tb7O12/TiO2 composite under ultrasonic irradiation.* Ultrasonics sonochemistry, 2011, **18**(3), 713-717.

[28] Moradi, V., Jun, M. B., Blackburn, A., & Herring, R. A., *Significant improvement in visible light photocatalytic activity of Fe doped TiO2 using an acid treatment process*. Applied Surface Science, 2018, **427**: P. 791-799.

[29] Stucchi, M., Cerrato, G., & Bianchi, C. L., *Ultrasound to improve both synthesis and pollutants degradation based on metal nanoparticles supported on TiO2.* Ultrasonics sonochemistry, 2019, **51**: P. 462-468.

[30] Umar, K., Haque, M. M., Muneer, M., Harada, T., & Matsumura, M., *Mo, Mn and La doped TiO2: synthesis, characterization and photocatalytic activity for the decolourization of three different chromophoric dyes*. Journal of Alloys and Compounds, 2013, **578**: P. 431-438.

[32] Binas, V. D., Sambani, K., Maggos, T., Katsanaki, A., & Kiriakidis, G., *Synthesis and photocatalytic activity of Mn-doped TiO2 nanostructured powders under UV and visible light.* Applied Catalysis B: Environmental, 2012,**113**: P. 79-86.

[33] Deng, Q. R., Xia, X. H., Guo, M. L., Gao, Y., & Shao, G., *Mn-doped TiO2 nanopowders with remarkable visible light photocatalytic activity*. Materials Letters, 2011, **65**(13): P. 2051-2054.

[34] Wang, L., Zhang, X., Zhang, P., Cao, Z., & Hu, J., *Photoelectric conversion performances of Mn doped TiO2 under> 420 nm visible light irradiation*. Journal of Saudi Chemical Society, **19**(5): P. 595-601.

[35] Gogate, P. R., *Cavitation: an auxiliary technique in wastewater treatment schemes*. Advances in Environmental Research, 2002, **6**(3): P. 335-358.

[36] Gedanken, A., *Using sonochemistry for the fabrication of nanomaterials*. Ultrasonics sonochemistry, 2004, 11(2): P. 47-55

[37] Noman, M. T., Wiener, J., Saskova, J., Ashraf, M. A., Vikova, M., Jamshaid, H., & Kejzlar, P., *In-situ development of highly photocatalytic multifunctional nanocomposites by ultrasonic acoustic method*. Ultrasonics sonochemistry, 2018, **40**: P. 41-56.

[38] Tabasideh, S., Maleki, A., Shahmoradi, B., Ghahremani, E., & McKay, G., *Sonophotocatalytic degradation of diazinon in aqueous solution using iron-doped TiO2 nanoparticles*. Separation and Purification Technology, 2017, **189**: P. 186-192.

[39] Karekar, S. E., Bhanvase, B. A., Sonawane, S. H., Deosarkar, M. P., Pinjari, D. V., & Pandit, A. B., *Synthesis of zinc molybdate and zinc phosphomolybdate nanopigments by an ultrasound assisted route: advantage over conventional method.* Chemical Engineering and Processing: Process Intensification, 2015, **87**, 51-59.

[40] Neppolian, B., Bruno, A., Bianchi, C. L., & Ashokkumar, M., *Graphene oxide based Pt–TiO2 photocatalyst: ultrasound assisted synthesis, characterization and catalytic efficiency.* Ultrasonics sonochemistry, 2012, **19**(1): P. 9-15.

[41] Jagannathan, M., Grieser, F., & Ashokkumar, M., *Sonophotocatalytic degradation of paracetamol using TiO2 and Fe3+*. Separation and Purification Technology, 2013, **103**: P. 114-118.

[42] Pinjari, D. V., Prasad, K., Gogate, P. R., Mhaske, S. T., & Pandit, A. B., *Synthesis of titanium dioxide by ultrasound assisted sol–gel technique: effect of calcination and sonication time*. Ultrasonics sonochemistry, 2015, **23**: P. 185-191.

[43] Wang, J., & Bai, Z., *Fe-based catalysts for heterogeneous catalytic ozonation of emerging contaminants in water and wastewater.* Chemical Engineering Journal, 2017, **312**: P. 79-98.

[44] Prasad, K., Pinjari, D. V., Pandit, A. B., & Mhaske, S. T., *Synthesis of titanium dioxide by ultrasound assisted sol–gel technique: effect of amplitude (power density) variation*. Ultrasonics sonochemistry, 2010, **17**(4): P. 697-703.

[45] Shende, T. P., Bhanvase, B. A., Rathod, A. P., Pinjari, D. V., & Sonawane, S. H., *Sonochemical synthesis of Graphene-Ce-TiO2 and Graphene-Fe-TiO2 ternary hybrid photocatalyst nanocomposite and its application in degradation of crystal violet dye.* Ultrasonics sonochemistry, 2018, **41**: P. 582-589.

[46] Behzadnia, A., Montazer, M., & Rad, M. M., *Simultaneous sonosynthesis and sonofabrication of N-doped ZnO/TiO2 core–shell nanocomposite on wool fabric: Introducing various properties specially nano photo bleaching.* Ultrasonics sonochemistry, 2015, **27**: P. 10-21.

[47] Gedanken, A., *Using sonochemistry for the fabrication of nanomaterials*. Ultrasonics sonochemistry, 2004, **11**(2), 47-55.

[48] Aziz, R. A., Yusof, N. M., & Masrom, A. K., *Effect of Ultrasonic Irradiation Time and Amplitude Variation on TiO2 Particles*. Solid State Sci. Technol., 2011, **19**: P. 371-383.

[49] Tripathi, A. K., Mathpal, M. C., Kumar, P., Singh, M. K., Soler, M. A. G., & Agarwal, A., *Structural, optical and photoconductivity of Sn and Mn doped TiO2 nanoparticles.* Journal of Alloys and Compounds, 2015, **622**: P. 37-47.

[50] Yu, J., Zhou, M., Cheng, B., Yu, H., & Zhao, X., *Ultrasonic preparation of mesoporous titanium dioxide nanocrystalline photocatalysts and evaluation of photocatalytic activity*. Journal of Molecular Catalysis A: Chemical, 2005, **227**(1-2): P. 75-80.

[51] Zhou, M., Yu, J., & Cheng, B., *Effects of Fe-doping on the photocatalytic activity of mesoporous TiO2 powders prepared by an ultrasonic method.* Journal of Hazardous Materials, 2006, **137**(3), 1838-1847.

[52] Neppolian, B., Wang, Q., Jung, H., & Choi, H., *Ultrasonic-assisted sol-gel method of preparation of TiO2 nano-particles: characterization, properties and 4-chlorophenol removal application.* Ultrasonics sonochemistry, 2008, **15**(4), 649-658.

[53] Li, H., Liu, G., Chen, S., & Liu, Q., *Novel Fe doped mesoporous TiO2 microspheres: ultrasonic–hydrothermal synthesis, characterization, and photocatalytic properties*. Physica E: Low-dimensional Systems and Nanostructures, 2010, **42**(6), 1844-1849.

[54] Stucchi, M., Bianchi, C. L., Argirusis, C., Pifferi, V., Neppolian, B., Cerrato, G., & Boffito, D. C., *Ultrasound assisted synthesis of Ag-decorated TiO2 active in visible light.* Ultrasonics sonochemistry, 2018, 40, 282-288.

[55] Skoog DA, Holler FJ, Crouch SR, *Principles of Instrumental Analysis*. 2007, Sixth Edition, Thomson Brooks, USA

[56] Sakurai, K., & Mizusawa, M., *X-ray diffraction imaging of anatase and rutile.* Analytical chemistry, 2010, **82**(9) : P. 3519-3522.

[57] Ambroz, F., Macdonald, T. J., Martis, V., & Parkin, I. P., Evaluation of the BET Theory for the Characterization of Meso and Microporous MOFs. Small Methods, 2018, 2(11): P. 1800173.

[58] Ye, Z., Jiang, X., & Wang, Z., *Measurements of Particle Size Distribution Based on Mie Scattering Theory and Markov Chain Inversion Algorithm*. JSW, 2012, **7**(10) : P. 2309-2316.

[59] Begum, R., Farooqi, Z. H., Naseem, K., Ali, F., Batool, M., Xiao, J., & Irfan, A., Applications of UV/Vis spectroscopy in characterization and catalytic activity of noble metal nanoparticles fabricated in responsive polymer microgels: a review. Critical reviews in analytical chemistry, 2018, 48(6): P. 503-516.

[60] López, R., & Gómez, R., *Band-gap energy estimation from diffuse reflectance measurements on sol–gel and commercial TiO2: a comparative study*. Journal of sol-gel science and technology, 2012, **61**(1): P. 1-7.

[61] Babu, Sundaram Ganesh, et al., *Synergistic effect of sono-photocatalytic process for the degradation of organic pollutants using CuO-TiO2/rGO*, Ultrasonics sonochemistry, 2019, **50**, P. 218-223.

[62] Miklos, David B., et al., *Evaluation of advanced oxidation processes for water and wastewater treatment–a critical review.*, Water Research, 2018, **139**, P. 118-131.

[63] Geng, Nannan, et al., *Preparation of Fe3O4/TiO2-N-GO sonocatalyst and using for humic acid removal with the assist of ultrasound.*, Materials Science in Semiconductor Processing, 2019, **102**, P. 104593.

[64] Stucchi, M., G. Cerrato, and C. L. Bianchi., *Ultrasound to improve both synthesis and pollutants degradation based on metal nanoparticles supported on TiO2.*, Ultrasonics sonochemistry, 2019, **51**, P. 462-468.